

Optimization of the
reconstruction codes for the
central inner z-chamber
at the H1 experiment

Diploma Thesis
of
Thomas M. Walter

carried out in the group of
Prof. Dr. P. Truöl
under supervision of
Dr. U. Straumann

July 1995

Physik-Institut der Universität Zürich

Optimization of the
reconstruction codes for the
central inner z-chamber
at the H1 experiment

Diploma Thesis
of
Thomas M. Walter

carried out in the group of
Prof. Dr. P. Truöl
under supervision of
Dr. U. Straumann

July 1995
Physik-Institut der Universität Zürich

Contents

1	Introduction	6
1.1	Physics at HERA	6
2	Deep inelastic scattering (DIS) at HERA	8
2.1	Kinematics of DIS	9
2.2	Determination of the kinematic variables	9
2.3	Electron-only-method	14
3	The H1 Experiment	15
3.1	The HERA machine	15
3.2	The H1 Detector	16
3.3	The central tracker	18
4	The central inner z-chamber CIZ	20
4.1	Operation principles of wire chambers	20
4.2	Operation principles of drift chambers	21
4.3	An overall view of the CIZ	22
4.4	Reconstruction of particle tracks in the CIZ	23
4.5	Determination of charge and time (Qt -analysis)	25
4.5.1	First electron method: the COZ- Qt -code	25
4.5.2	Differences between the CIZ- and COZ- Qt	27
5	Investigations pertaining to the charge and time analysis codes	28
5.1	Problems of the charge-time analysis	28
5.1.1	Lost hits	28

5.1.2	Time structure	29
5.2	Comparison between the different charge-time analyses	30
5.2.1	The event selection	30
5.2.2	Determination of the efficiency	31
5.2.3	Comparison of the φ -resolution	34
5.2.4	Comparison of the z -resolution	36
5.3	Conclusions	37
6	Investigations pertaining to the ϑ-resolution	38
6.1	Introduction	38
6.2	Data processing	40
6.2.1	Event selection	40
6.2.2	The different version of deducing the scattering angle ϑ	41
6.3	ϑ -resolution in data and simulation	42
6.4	Non-Gaussian tails in the ϑ -resolution	47
6.5	Conclusions	52
6.5.1	Estimation of the errors of x and Q^2	52

Abstract

At HERA (Hadron Electron Ring Accelerator), the electron-proton storage ring at DESY (Deutsches Elektronen Synchrotron) in Hamburg (Germany), particles are accelerated and stored in two separate rings. Two detectors, H1 and Zeus, were built around the collision points of the electrons and protons.

The reaction products are measured with many different detector components. The two innermost parts, the CIP (Central Inner Proportional chamber) and the CIZ (Central Inner Z-chamber) were built at the "Physik-Institut der Universität Zürich".

The identification of every single particle and the determination of their energy and momentum is called event reconstruction. This thesis investigates whether the first step of the CIZ-reconstruction can be optimized. In the second part, the influence of the CIZ on deducing the kinematics of an event is studied, i. e. how much the reconstruction of the kinematic variables can be improved by using the CIZ.

Zusammenfassung

In HERA (Hadron Elektron Ring Anlage), dem Elektron-Proton-Speicherring am Deutschen Elektronen-Synchrotron (DESY) in Hamburg, werden in zwei übereinanderliegenden Ringen Teilchen beschleunigt und gespeichert. Zwei Detektoren, H1 und Zeus, wurden um die Kollisionpunkte der Elektronen und Protonen aufgebaut.

Die Reaktionsprodukte werden mit vielen verschiedenen Detektorkomponenten ausgemessen. Die zwei innersten Komponenten, die CIP (Central Inner Proportional chamber) und die CIZ (Central Inner Z-chamber), wurden am Physik-Institut der Universität Zürich gebaut.

Die Teilchen müssen identifiziert und deren Energie und Impuls bestimmt werden. Dies nennt man 'Rekonstruktion des Ereignisses'. In dieser Diplomarbeit wurde untersucht, ob man den allerersten Rekonstruktionsschritt der CIZ optimieren kann. Im zweiten Teil wurde der Einfluss der CIZ auf die Ermittlung der Kinematik eines Ereignisses studiert. Mit anderen Worten, es wurde untersucht, wieviel genauer die kinematischen Variablen mit Hilfe der CIZ rekonstruiert werden können.

Chapter 1

Introduction

Most of our knowledge about the structure of matter was gained by scattering experiments. After Rutherford discovered nuclei, further investigations showed that they are composed of protons and neutrons. At HERA (Hadron Elektron Ring Anlage), this research is continued to determine the substructure of protons.

In the late sixties, deep inelastic lepton nucleon scattering at SLAC (Stanford Linear Accelerator) showed that protons are composed of point-like objects called partons [1]. In the quark-parton-model partons are identified with quarks carrying spin $\frac{1}{2}\hbar$ and a charge of multiples of one third of the elementary charge e [2]. Further experiments showed that the nucleon consists not only of quarks but also of gluons, which are the exchange particles of the strong interaction. Gluons and sea quarks carry half of the momentum of the nucleon.

1.1 Physics at HERA

To reach a much higher center of mass energy compared to previous fixed target experiments, the first electron proton collider HERA was built at DESY (Deutsches Elektronen Synchrotron, Hamburg). In a 6.3 km long circular tunnel, two independent rings for accelerating and storing electrons and protons have been installed. Protons, with an energy of 820 GeV, collide with electrons, with an energy of 27 GeV, at the two interaction zones in the Hall North and South, thus resulting in a center of mass energy of about 300 GeV, two orders of magnitudes higher than in previous experiments.

The scattering amplitude is dominated by the processes shown in Figure 1.1a) and b): An electroweak gauge boson is exchanged between the electron and a quark inside the proton. The high center of mass energy allows a very high momentum transfer, making the weak exchange boson Z_0

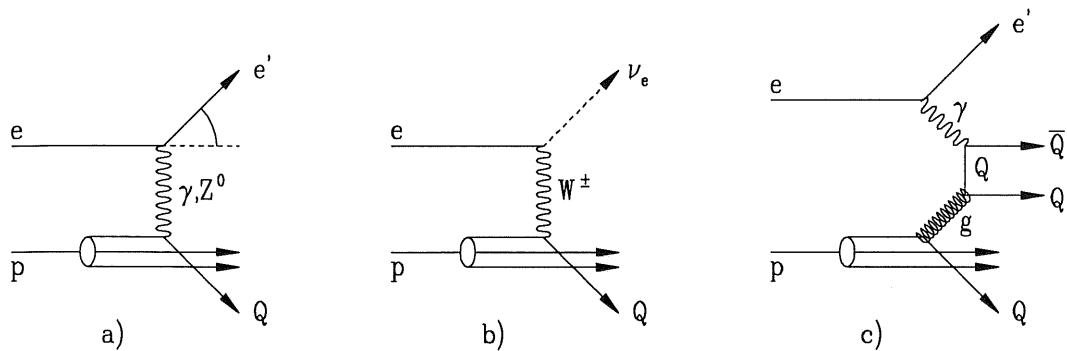


Figure 1.1: Feynman diagrams for the basic processes studied at HERA (from [4])

visible and resolving structures down to 10^{-18} m. On the other hand, it allows to observe partons inside the proton at very low x , x being the fraction of the proton momentum carried by struck quark.

The main points of interest are the following:

- “How does it look like inside a proton?” In particular, the proton structure function at low x and high Q^2 , a kinematical range uncovered by previous experiments, is being investigated (see Figure 1.1a).
- The total photoproduction cross section where an almost real photon is exchanged ($Q^2 \approx 0$). This gives information about the content of photons as well as the content of protons.
- Testing the electroweak theory with charged current events (instead of a photon a W^- or W^+ vector boson is exchanged) (see Figure 1.1b).
- Strong interaction processes like QCD-compton or gamma-gluon fusion [production of heavy quark mesons (D 's, J/Ψ , ...)] (see Figure 1.1c).

Thus HERA opens the door to new physical regions with special significance for understanding the structure of matter at very small dimensions and the relevant theory behind it: Quantum Chromodynamics (QCD) [3].

A detailed introduction to the physics at HERA is compiled in [4, 5].

Chapter 2

Deep inelastic scattering (DIS) at HERA

Due to the very high center of mass energy at HERA we can resolve structures down to 10^{-18} m.

$$\begin{aligned}
 E &= \hbar\omega = \frac{hc}{\lambda} \\
 \Rightarrow d_{min} &= \frac{hc}{E_{max}} = \frac{hc}{\sqrt{s}} \approx 10^{-18} \text{ m}
 \end{aligned}
 \tag{2.1}$$

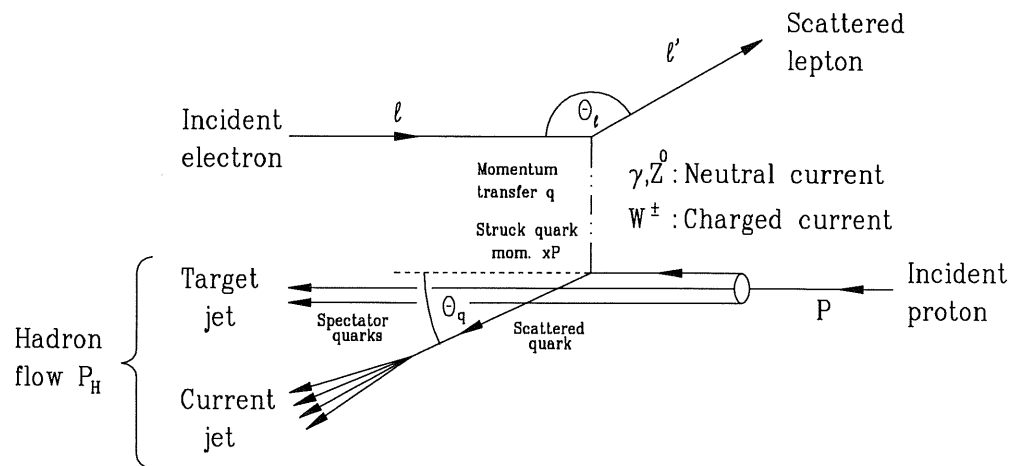


Figure 2.1: Basic diagram for deep inelastic scattering (from [9])

2.1 Kinematics of DIS

In DIS a gauge boson of the electroweak interaction (γ , Z_0 or W^\pm) (see Figure 1.1 and 2.1) is exchanged. The scattering process can be described as follows: $e + p \rightarrow l + H$, where e stands for the incoming electron, p for the proton, l for the scattered lepton, and H denotes the hadron final state.

$$k = \begin{pmatrix} E_e \\ \vec{p}_e \end{pmatrix} \quad P = \begin{pmatrix} E_p \\ \vec{p}_p \end{pmatrix} \quad k' = \begin{pmatrix} E_l \\ \vec{p}_l \end{pmatrix} \quad H = \begin{pmatrix} E_H \\ \vec{p}_H \end{pmatrix}$$

If the masses of the electron and proton can be neglected, the total invariant mass squared s is given by the following formula:

$$s = (k + P)^2 = (k' + H)^2 \approx 4 \cdot E_e E_p = 4 \cdot E_l E_H \quad (2.2)$$

The comparison of measurements of different experiments is difficult, if one describes the result as a function of energy and scattering angle. More appropriate are the Lorentz invariant variables x, y and Q^2 .

$$\begin{aligned} Q^2 &:= -q^2 &:= -(k - k')^2 &= -(P - H)^2 \\ y &:= \frac{q \cdot P}{k \cdot P} \\ x &:= \frac{Q^2}{2P \cdot q} \\ Q^2 &= xys \end{aligned} \quad (2.3)$$

Q^2 is the negative square of the four momentum transferred from the electron to the proton, or, with other words, the absolute value of the mass squared of the exchanged particle. In the quark parton model, x is interpreted as the momentum fraction of the proton carried by the struck quark. The relative energy loss of the electron in the rest frame of the proton is given by y .

2.2 Determination of the kinematic variables

On the assumption that the beam energies (E_e, E_p) are known, one needs only two variables to describe the scattering process. Neglecting the electron and proton masses, the four momenta of the incoming electron k , the proton P , the scattered lepton k' and final hadronic system P_J are [assuming the scattering process takes place in the x - z -plane]:

$$k = \begin{pmatrix} E_e \\ 0 \\ 0 \\ -E_e \end{pmatrix} \quad k' = \begin{pmatrix} E' \\ E' \sin \vartheta \\ 0 \\ E' \cos \vartheta \end{pmatrix} \quad P = \begin{pmatrix} E_p \\ 0 \\ 0 \\ E_p \end{pmatrix} \quad P_J = \begin{pmatrix} E_J \\ -E_J \sin \gamma \\ 0 \\ E_J \cos \gamma \end{pmatrix} \quad (2.4)$$

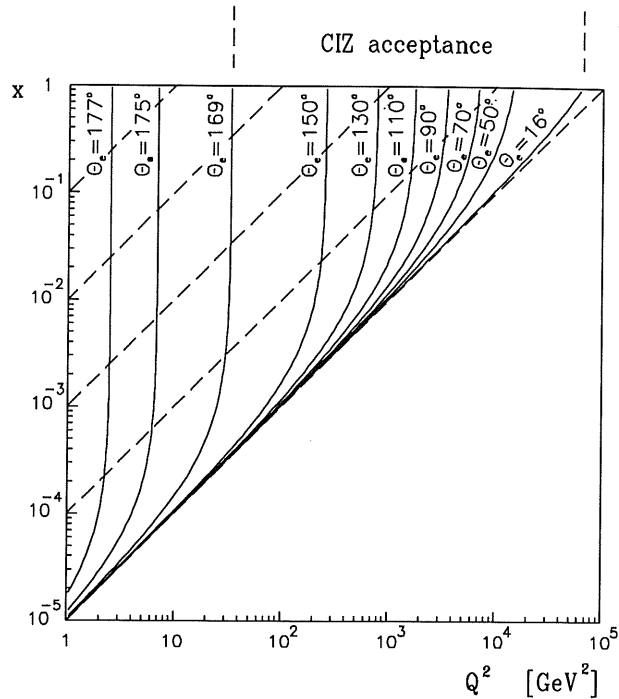


Figure 2.2: Lines of constant electron scattering angle (from [9]). Lines of constant y are shown dashed. The angular acceptance of the CIZ reaches from $\vartheta = 16^\circ$ to $\vartheta = 169^\circ$.

The H1 detector measures the energy and the angle of both the scattered electron and of the hadronic final state. With these four measured quantities, the kinematic is over-determined. Therefore we have redundant information for reconstructing the kinematic variables, which is useful for estimating systematical errors. Figures 2.2-2.5 show (in the kinematical plane of x and Q^2) lines of constant energy or angle of the scattered electron or the jet, respectively. In the following the term 'jet angle' is used for the energy weighted average angle of the hadronic final state. This quantity is well defined even if the hadrons do not form a jet like object. The most important features are:

- (2.2) Lines of constant electron scattering angle: because the ϑ -lines are almost parallel to the x -axis the x determination only depends weakly on the ϑ -resolution, while at very high Q^2 the ϑ -dependence of x is stronger. Events at very low Q^2 ($Q^2 < 4\text{GeV}$) are lost since the electron escapes through the beampipe.
- (2.3) Lines of constant scattered electron energy: a large kinematic region between 25 and 30 GeV is practically insensitive to the electron energy.

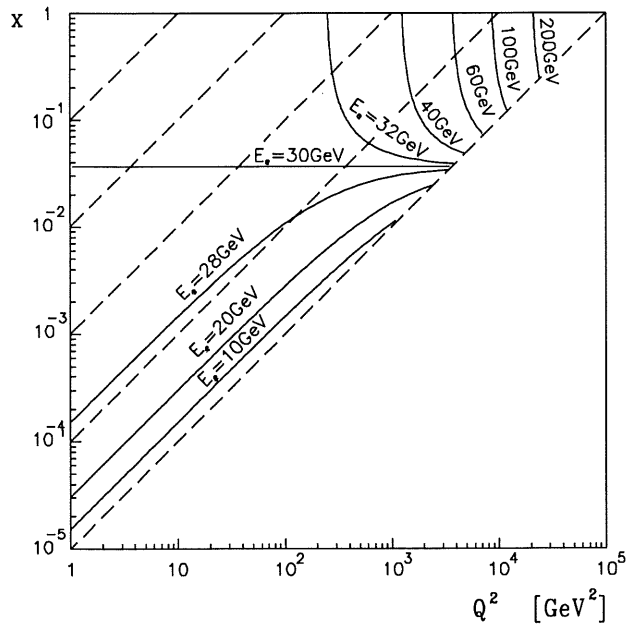


Figure 2.3: Lines of constant scattered electron energy (from [9]) (Drawn for the electron design energy of 30 GeV)

This makes a determination of x using the electron energy for $y < 0.1$ (lowest dashed line) more difficult.

- (2.4) Lines of constant jet angle: in the region of very low x , the jet starts pointing backwards, leading to misidentification of hadrons and the electron. In order to minimize these misidentification the BEMC (Backward ElectroMagnetic Calorimeter, see Figure 3.2 (12)) was replaced in 1995 by the SPACAL (SPAGhetti CALorimeter) which consists of an electromagnetic and a hadronic part. Hence, hadrons are recognized by the deposited energy in the hadronic part.
- (2.5) Lines of constant hadronic energy: the region at very low x and low Q^2 cannot be used because the accuracy of the energy measurement is not good enough.

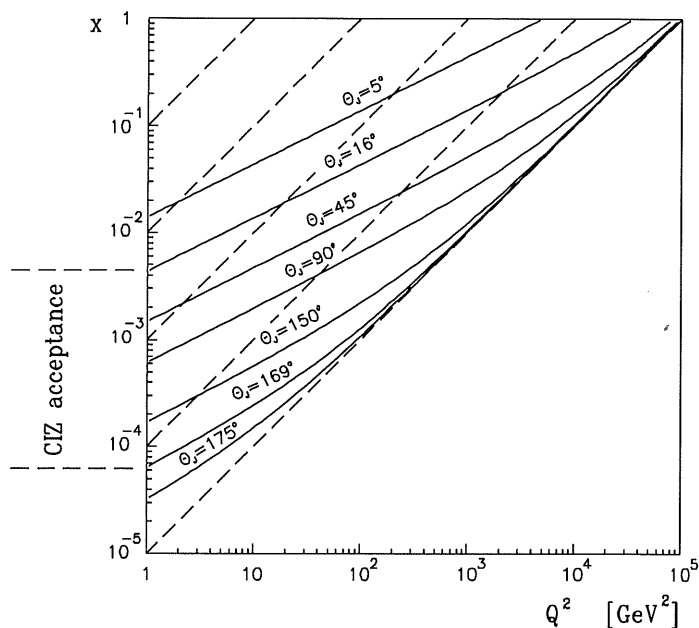


Figure 2.4: Lines of constant current jet angle (from [9]). The angular acceptance of the CI-Z reaches from $\vartheta = 16^\circ$ to $\vartheta = 169^\circ$.

The four observables provide six different methods of reconstructing x , y and Q^2 . Because of further investigations on the ϑ -resolution in this thesis, the electron-only-method will be discussed in greater detail. Other methods are described in [7] and [8], for example.

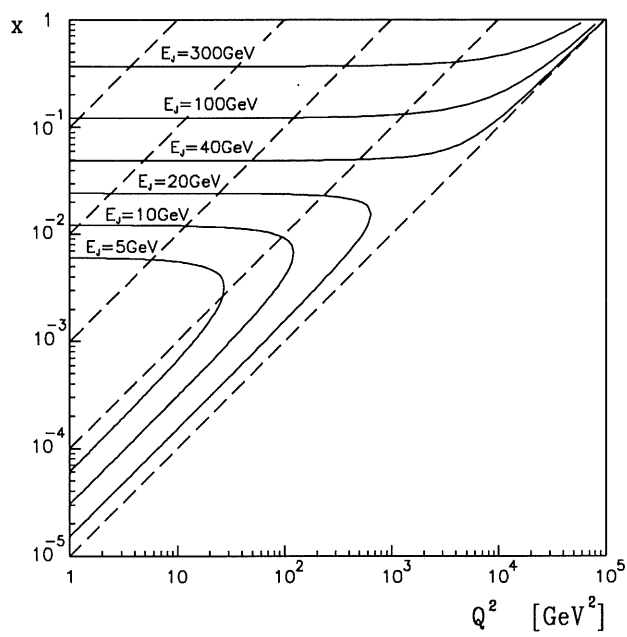


Figure 2.5: Lines of constant current jet energy (from [9])

2.3 Electron-only-method

Conventionally, the kinematical variables x, y and Q^2 are deduced from the measurement of the energy and the angle of the scattered electron, especially in the previous fixed target experiments. By putting the four momenta from above (2.4) into the definition of x, y and Q^2 (2.3), and by neglecting the masses of the electron and the proton, we get the following expressions for the kinematic variables:

$$Q^2 = 4E_e E' \cos^2 \frac{\vartheta}{2} \quad y = 1 - \frac{E'}{E_e} \sin^2 \frac{\vartheta}{2} \quad x = \frac{Q^2}{sy} \quad (2.5)$$

The dependence of the reconstructed Q^2 and x on the measurement errors of the laboratory quantities can be expressed by means of the partial derivatives:

$$\frac{\delta Q^2}{Q^2} = \sqrt{\left(\frac{dE'}{E'}\right)^2 + \left(\tan \frac{\vartheta}{2} d\vartheta\right)^2} \quad (2.6)$$

$$\frac{\delta x}{x} = \sqrt{\left(\frac{1}{y} \frac{dE'}{E'}\right)^2 + \left(\tan \frac{\vartheta}{2} \left(x \frac{E_p}{E_e} - 1\right) d\vartheta\right)^2} \quad (2.7)$$

The electron energy resolution in the calorimeter is typically $\frac{dE}{E} = \frac{12\%}{\sqrt{E [\text{GeV}]}}$ (see [6]) and the angular measurement accuracy is about $d\vartheta = 1$ mrad (see section 6).

From these equation, we can easily observe that:

- The resolution in Q^2 is very good (a few percent) except for very small scattering angles (i.e. large ϑ) where the angular precision becomes the dominant term.
- The error of x due to the angular precision is only significant at large x or at very low Q^2 (large ϑ).
- The resolution of x at low y is very poor because of the factor $\frac{1}{y}$ in the energy error. Therefore, with our calorimeter accuracy, it is practically impossible to measure x at y below 0.1 with the electron-only-method.

Chapter 3

The H1 Experiment

The H1 Experiment is a collaboration of about 350 scientists from 37 different research institutes in 11 countries. It is one of four experiments at the interaction zones at HERA, a particle accelerator and storage ring at DESY. The others are Zeus, Hermes and HERA-B.

3.1 The HERA machine

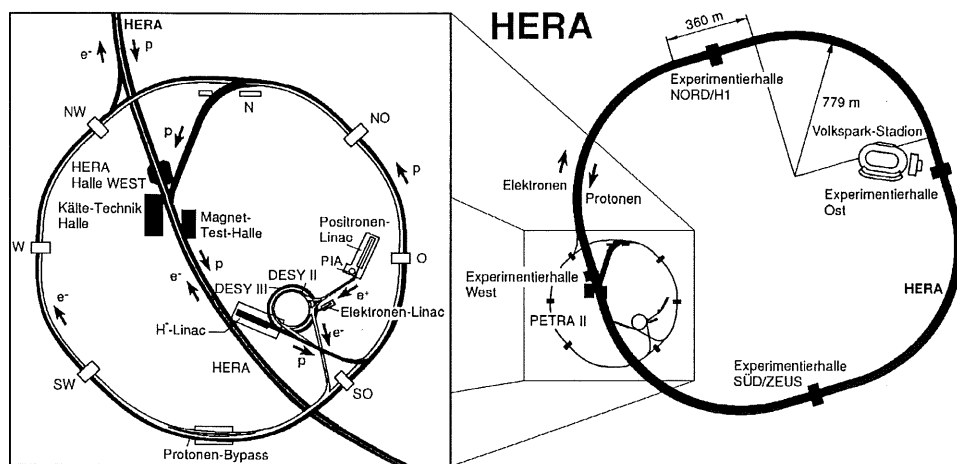


Figure 3.1: The HERA storage ring

HERA is a complex system for accelerating, storing and colliding electrons and protons situated in a 6.3 km long circular tunnel. Figure 3.1 gives an overview of the HERA storage ring, the injection chain and the location

of the experiments. In the summer of 1994 the machine was switched from using electrons to positrons in order to increase the beam lifetime. Thus, if in the text beam electrons are mentioned, positrons are always implicitly meant, too.

The electron machine is a conventional storage ring, accelerating the electrons up to 27 GeV, whereas the proton machine makes use of superconducting magnets to produce the high magnetic field needed to keep the 820 GeV protons in their orbit. In contrast to the proton ring, where the limit for the beam energy is the maximal achievable magnetic field, the limiting factor for the electron energy is given by the energy loss through synchrotron radiation. The electrons and protons are pre-accelerated in the former e^+e^- storage ring PETRA up to an injection energy of 12 GeV and 40 GeV, respectively.

The particles are grouped together into a maximum of 220 bunches, leading to a bunch crossing distance of only 96 ns. They are brought to head-on collisions in the hall north (H1) and south (ZEUS). The experiments HERMES (hall east) and HERA-B (hall west) use the electron or the proton beam, respectively.

In the 1994 running period 170 of the proton bunches and 168 of the electron bunches were filled, 153 were colliding. Bunches with no colliding partner were used to estimate the background induced by the beam.

3.2 The H1 Detector

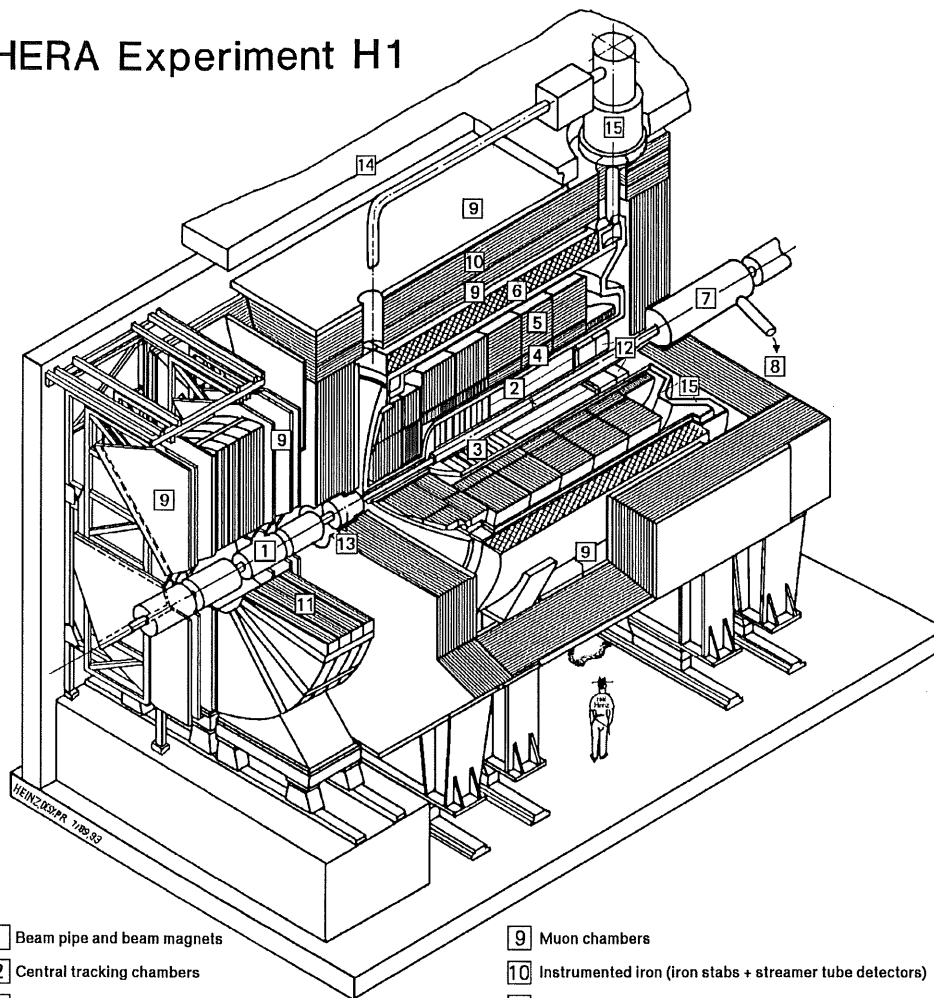
Figure 3.2 gives an overview of the H1 detector. The large imbalance in the energy of the two colliding beams, which boosts the center of mass system along the proton flight direction, is a major design condition. It leads to asymmetric construction of the overall detector and to a much finer granularity in forward direction (i. e. the direction of the outgoing proton) than in the backward region.

For the best possible identification of the different interaction products, the detector consists of several independent components. Let's start the description from the interaction point.

The tracking system, used for the determination of momentum and angle of charged particles, is located in the core of the detector. Because of the asymmetry of the electron and proton beam energy many charged particles are produced at small angles ϑ to the forward direction. To maintain a good efficiency over the whole solid angle, the tracker is divided into two mechanically distinct units, the central (2)¹ and forward (3) parts, each

¹The following numbers refer to Figure 3.2

HERA Experiment H1



- | | | | |
|---|---|----|--|
| 1 | Beam pipe and beam magnets | 9 | Muon chambers |
| 2 | Central tracking chambers | 10 | Instrumented iron (iron stabs + streamer tube detectors) |
| 3 | Forward tracking and Transition radiators | 11 | Muon toroid magnet |
| 4 | Electromagnetic calorimeter (lead) | 12 | Warm electromagnetic calorimeter |
| 5 | Hadronic calorimeter (stainless steel) | 13 | Plug calorimeter (Cu, Si) |
| 6 | Superconducting coil (1.2T) | 14 | Concrete shielding |
| 7 | Compensating magnet | 15 | Liquid Argon cryostat |
| 8 | Helium cryogenics | | |
- } Liquid Argon

Figure 3.2: The H1 Detector

optimized for triggering and tracking in its angular region. Both contain several layers of drift and proportional chambers.

The calorimeter surrounding the trackers measures the energy of charged and neutral particles with the exception of high energy muons and neutrinos which cross the calorimeter practically unimpeded. It consists of the liquid argon (LAr) (4,5), the backward electromagnetic (BEMC) (12) and the plug (13) calorimeter.

A superconducting coil producing a magnetic field of 1.15 Tesla, is arranged around the track chambers and the calorimeter. Therefore, the particle tracks are curved, and their transversal momentum can be determined. The iron yoke (10) of the magnet is laminated and filled with streamer tubes for identifying muons. Very stiff muon tracks in forward direction are further analyzed by the muon toroidal magnet sandwiched between drift chambers.

The electron tagger at position $z = -33$ m upstream from the interaction point detects electrons with a very small scattering angle. In conjunction with the photon detector at $z = -103$ m it monitors the luminosity by the bremsstrahlung process $ep \rightarrow ep\gamma$. This reaction has a well known cross section.

A description of the H1 detector in much greater detail can be found in [6].

3.3 The central tracker

A short overview of the different chamber types is given in section 4.1. A more detailed introduction can be found in [9].

The track reconstruction in the central part is based on two large concentric drift chambers, the CJC1 and CJC2 (Central Jet Chamber). They have wires strung parallel to the beam axis. Therefore, we have a very good space resolution about $170 \mu\text{m}$ in the $r\varphi$ -plane (see section 4.2). In the z -direction we achieve only a resolution of a few percent of the wire length of 2.2 m.

Using the CJC in combination with the strong magnetic field and the therefore curved particle tracks, we can measure the transversal track momentum. Additionally, the specific energy loss $\frac{dE}{dx}$ is used for particle identification up to about 1 GeV.

To receive fast triggering signals over the full solid angle, the tracker is equipped with several multiwire proportional chambers (MWPC). In the central part, these are the innermost chamber CIP (Central Inner Proportional chamber) and the COP (Central Outer Proportional chamber), located between the CJC1 and CJC2.

Two thin drift chambers, the central inner (CIZ) and the central outer (COZ) z -chambers complement the central tracker. They determine the z -

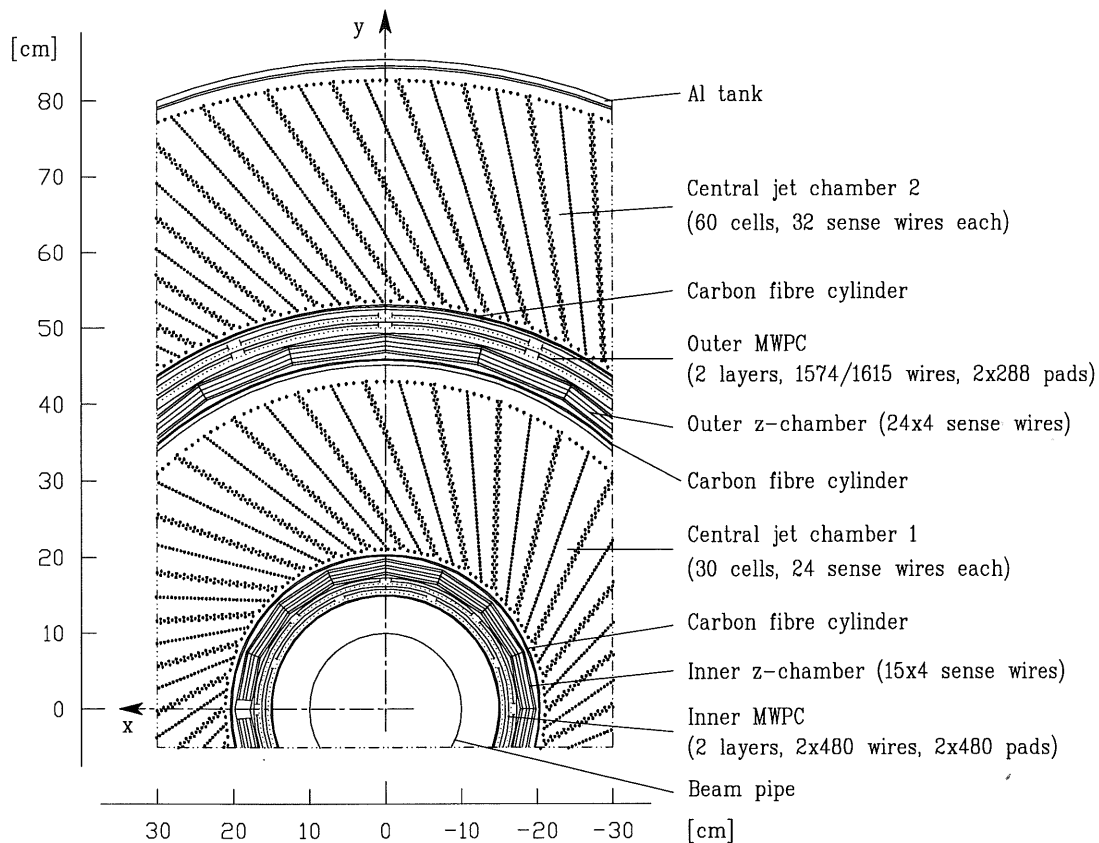


Figure 3.3: The central tracking system, section perpendicular to the beam (from[9])

coordinate of the tracks with high accuracy. This is crucial for a precise measurement of the angle ϑ of the scattered electron, which in combination with the energy E' defines the kinematics of the event. Since the z -chambers are essential also for reconstructing the z -coordinate of the event vertex, their measuring precision influences the accuracy of the determination of the event kinematics significantly.

Chapter 4

The central inner z -chamber CIZ

4.1 Operation principles of wire chambers

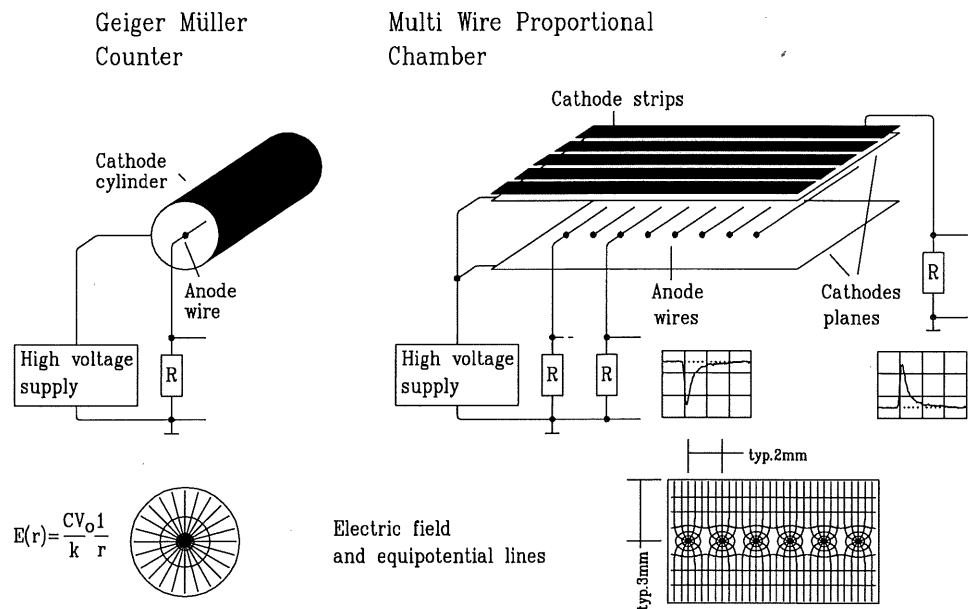


Figure 4.1: From the Geiger Müller counter to the multiwire proportional chamber (from [9])

The first wire chamber is the famous Geiger Müller counter, invented in 1908. It consists of a metallic cylinder containing an ionizing gas and a single anode wire strung along the axis kept at high voltage (see Figure 4.1). If a particle

passes through the cylinder it ionizes some gas molecules. The liberated electrons are then accelerated in the electric field to energies high enough to produce secondary electrons. They are finally collected at the anode wire while the positive ions move towards the cylinder. For very high voltages, the avalanche fully discharges the potential difference. This is called the “Geiger” mode, where one only needs a loudspeaker to hear the signal.

For lower voltage, the anode signal is proportional to the initial ionization with a multiplication factor of order 10^3 to 10^5 for every primary electron. Georges Charpak built the first multiwire proportional chamber (see Figure 4.1). The primary electrons drift in the electric field towards the nearest anode wire. The avalanche only begins about $50 \mu\text{m}$ before the wire because only there the field is strong enough to ionize further atoms. By electrostatic inductance a positive pulse can be discerned on the cathode as well as on the adjacent wires. Segmenting the cathode planes into strips running perpendicular to the anode wires enables locating the avalanche in two dimensions. The pulses can be recorded within about 20 ns after the particle passage. The actual time resolution of the chamber depends on the geometry because the primary electrons have to drift a certain distance to the anode wire before producing the signal.

4.2 Operation principles of drift chambers

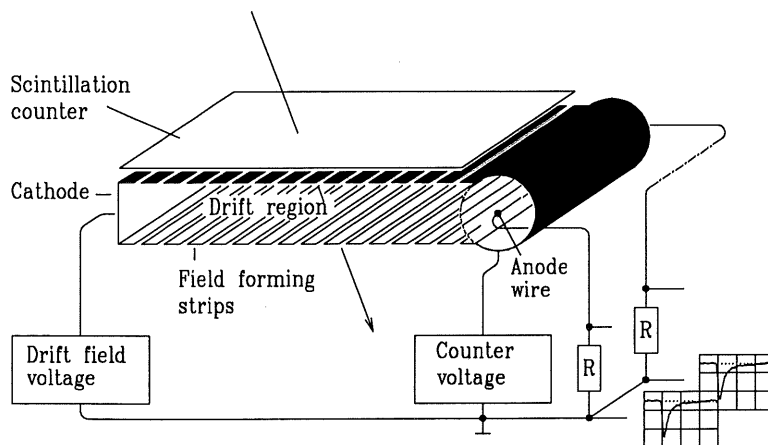


Figure 4.2: Scheme of a drift chamber (from [9])

The spacing between the wires does not need to be the limit of spatial resolution. With the measurement of the time delay it is possible to determine the origin of the primary electrons more precisely. In a drift chamber the electrons typically drift for about several centimeters in a low electric field

before they reach the anode wire at the time t_A . The distance of closest approach to the anode wire at time t_0 is given by:

$$z = \int_{t_0}^{t_A} v_D(t) dt \quad (4.1)$$

$v_D(t)$ is the drift velocity, which is essentially proportional to the electric field E at constant pressure p ($v_D \propto E$). A careful choice of the field configuration results in a more or less constant field and the equation (4.1) becomes linear:

$$z = v_D \cdot (t_A - t_0) = v_D \cdot \Delta t \quad (4.2)$$

Not only the drift and diffusion of the electrons and ions in the electromagnetic field determines the spatial resolution, but also the primary ionization process, the gas amplification near the anode wire and the time resolution of the read-out electronics.

4.3 An overall view of the CIZ

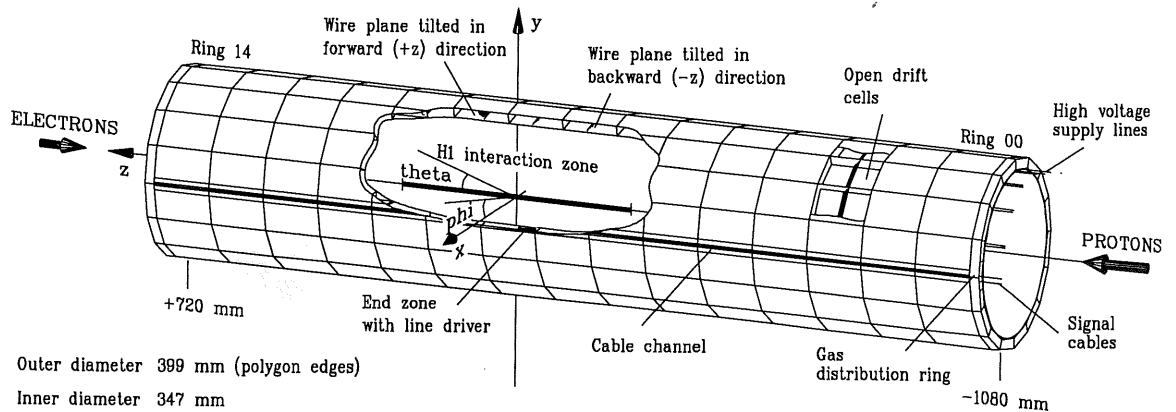


Figure 4.3: The central inner z -chamber CIZ (from [9])

The purpose of the z -chambers is, as the name suggests, the accurate measurement of the z -coordinate. This requires a drift direction parallel to the beam axis and sense wires perpendicular to the beam axis. The wires are strung as a sixteen-fold polygon around the beam, with an average radius of about 18 cm. To limit the drift distance, the chamber is divided into fifteen rings of 12 cm length (giving a total length of 1.8 m), each containing four sense (anode) and three fieldforming (potential) wires. The independent rings are separated by the printed circuit boards serving as cathode planes.

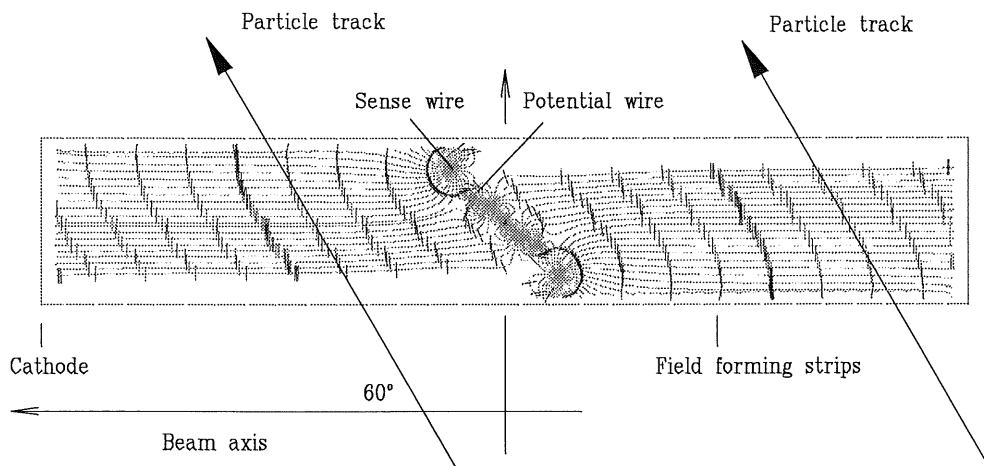


Figure 4.4: Isochrones and drift directions in the CIZ (from [9])

Since the CIZ is the innermost drift chamber, tracks cross it at a large range of angles, from 20° up to 170° . The best spatial resolution of a drift chamber is given for tracks parallel to isochrones (lines with equal drift time). It is desirable thus, that the isochrones point towards the interaction point. For this reason, the wire planes are tilted 45° backwards in the first nine rings and in ring 9–14 in forward direction. As a consequence the isochrones have a slope of about 60° relative to the beam axis (see Figure 4.4). This tilt results in another positive effect: The outer anode wire collects charge practically only from one side, which resolves the ambiguity whether the particle traversed the chamber on the right or on the left side of the wire plane.

4.4 Reconstruction of particle tracks in the CIZ

If a particle crosses a drift chamber a voltage pulse develops on the sense wire as explained above in section 4.1. These pulses are read out on both wire ends with FADC's (Flash Analog to Digital Converter). To determine the spatial coordinates of the particle from the digitized pulse, several steps are needed.

These steps are performed within a computer code which primarily yields the total integrated charge "Q" and the arrival time "t", and hence is often called Qt-code. While the arrival time "t" yields the coordinate perpendicular to the wire, i. e. z , the charge "Q" leads to the coordinate along the wire, i. e. φ , as will be explained below.

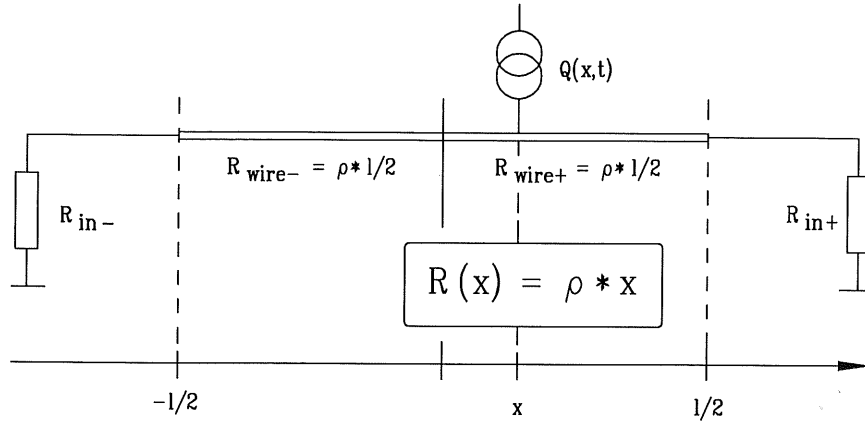


Figure 4.5: Illustration of the charge division mechanism (from [9])

The longer the distance between the hit point of the avalanche on the wire and the wire end is, the weaker is the recorded pulse. The signals are attenuated linearly due to the ohmic resistance, i. e. linear to the wire length. (This is only true if one can neglect electromagnetic wave characteristics, i. e. if the total ohmic resistance is larger than the critical resistance: $\rho l = R > R_{crit} := 2\pi\sqrt{\frac{L}{C}}$). This effect is utilized to determine the coordinate along the wire out of the ratio of the measured charge on both wire ends (See Figure 4.5).

$$\begin{aligned} \frac{Q_+}{Q_-} &= \frac{R_-}{R_+} = \frac{R_{wire-} + \rho x + R_{in-}}{R_{wire+} - \rho x + R_{in+}} \\ \Rightarrow x &= \frac{1}{\rho} \frac{Q_+ (R_{wire+} + R_{in+}) - Q_- (R_{wire-} + R_{in-})}{Q_+ + Q_-} \end{aligned} \quad (4.3)$$

- $R_{wire.}$: $\frac{1}{2}$ ohmic resistance of the wire
- ρ : specific ohmic resistance of the wire
- $R_{in.}$: input resistance of the preamplifier

The reconstruction in the coordinate plane perpendicular to the wire (i. e. parallel to drift direction) is much more difficult, but the resolution is far better. First, the drift time of the electrons has to be determined. Unfortunately, there is no linear relation between the drift time and the coordinate. It strongly depends on the track slope in the $r\phi$ -plane. In the final reconstruction the hits are deduced from the drift time, the track slope and the so called isochrone map, i. e. a map containing sample curves of equal drift time (see Figure 4.4).

The charge ratio can be determined less accurately than the drift time. Thus, the primary use of drift chambers is to measure accurately the coordinate perpendicular to the sense wires. The other coordinate along the wire is

solely required to link the hits of the different chambers to the right particle track.

Sometimes the CIZ “sees” more pulses than Qt -routine is able to digest. This and other undesirable effects [and whether they are remediable with different versions of Qt -codes] will be discussed in section 5.

4.5 Determination of charge and time (Qt -analysis)

At the H1 experiment, the Qt -routines are running online, i. e. as soon as the chambers are read out, the raw data is analyzed. Afterwards only the extracted charge and time values are stored, while the huge amount of raw data is discarded. For that reason, the correct values cannot be reconstructed off-line if there was an error in the charge-time analysis. Therefore, it is especially important that the pulses are recognized properly from the very beginning. The Qt -procedure has to be fast because we do not have that much computing power online and even more important, we want to reduce the dead-time to a minimum.

4.5.1 First electron method: the COZ- Qt -code

As already mentioned above, the Qt -routine determines the integrated charge on the left and the right wire end as well as the drift time. There exist basically two different approaches to determine “Q” and “t” — the first-electron-method and the center of gravity method. The first method is employed in the Qt -code used in the central outer z -chamber (see section 3.3).

To process a typical pulse, such as illustrated in Figure 4.6, the following steps are executed in the COZ- Qt -code:

- The pedestal (DC-offset without pulse) V_0 is estimated in a number (typically 12) of so called prebins. (1 bin = 9.6 ns) (see Figure 4.6: area h)
- The starting point of the pulse t_i is defined by two adjacent bins exceeding the threshold i , and it ends (t_k) as soon as two successive bins are below the value k .
- If the distance $t_k - t_i$ between the beginning and the end is shorter than m (e.g. 5 bins), the pulse is rejected.

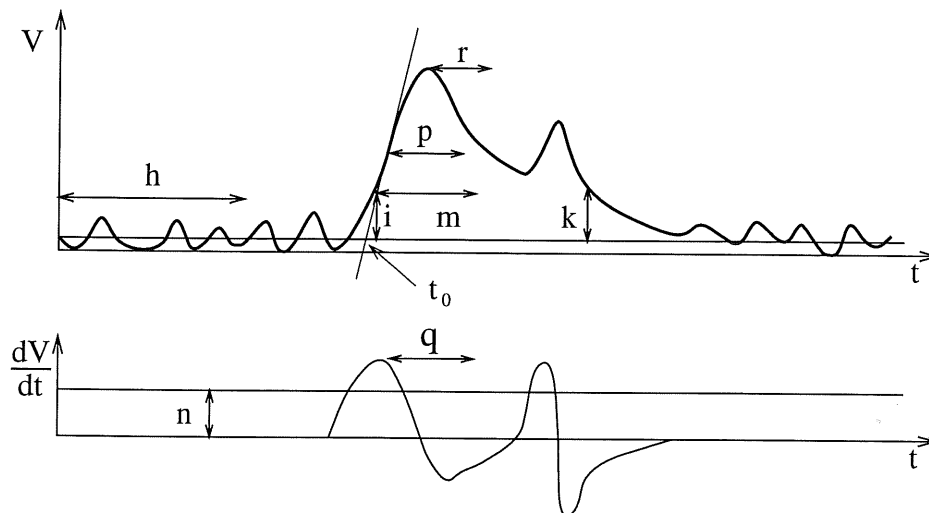


Figure 4.6: Scheme of the Qt -analysis

- Searching the peak of the pulse is done on the sum of the right and left channel, i.e. only one common peak position for both channels is determined.
- The differentiated pulse has to be higher than n to be accepted.
- Additionally required is a minimal width p at the half height (typically 5 bins).
- A straight line is fitted to three points in the steepest part of the peak slope for extrapolating back to the starting point t_0 . t_0 is the a measure of the arrival time of the first electron, which explains the name “first-electron-method (FEL)”.
- If two peaks separated by at least q channels are seen, they are treated as two different pulses and an exponential decay of the first is subtracted from the second one.
- For the charge determination the pulse is not integrated over the whole length, but only until r bins after the peak.

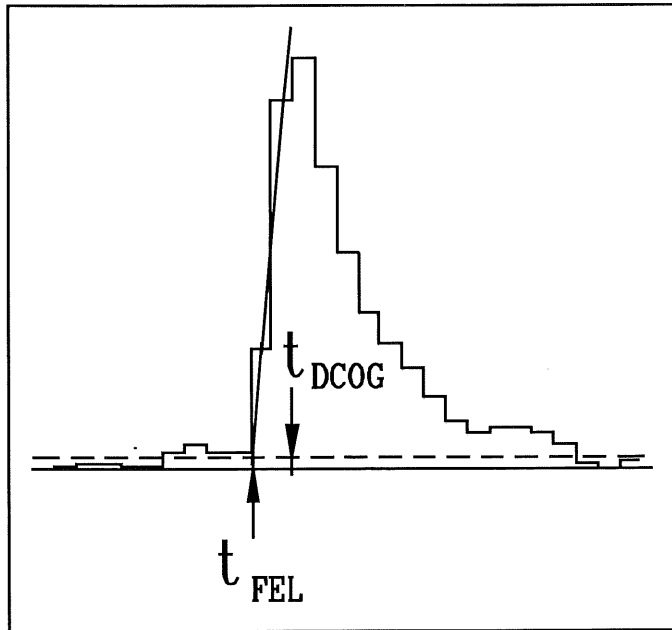


Figure 4.7: The two main methods for the pulse time determination. The first electron method (FEL) fits a straight line into the peak slope for extrapolating the beginning of the pulse. The DCOG-method (differential center of gravity) defines the time of the pulse as the center of gravity of the pulse rise.

4.5.2 Differences between the CIZ- and COZ- Qt

There are two main differences between the CIZ- and the COZ- Qt :

- In the CIZ- Qt , the time is determined with the differential center of gravity method (DCOG) instead of the first-electron-method. In this method the differences between adjacent channels from the start of the pulse to the peak position are computed. The drift time is then defined as the center of gravity of these differences (see Figure 4.7). The two methods have different time-constant t_0 .
- With the CIZ- Qt , the charge is integrated over the whole pulse. In contrast, the COZ- Qt integrates only over certain amount of bins after the peak. With the confinement to a few bins one gains a better φ resolution, as shown in section 5.7.

Chapter 5

Investigations pertaining to the charge and time analysis codes

5.1 Problems of the charge-time analysis

5.1.1 Lost hits

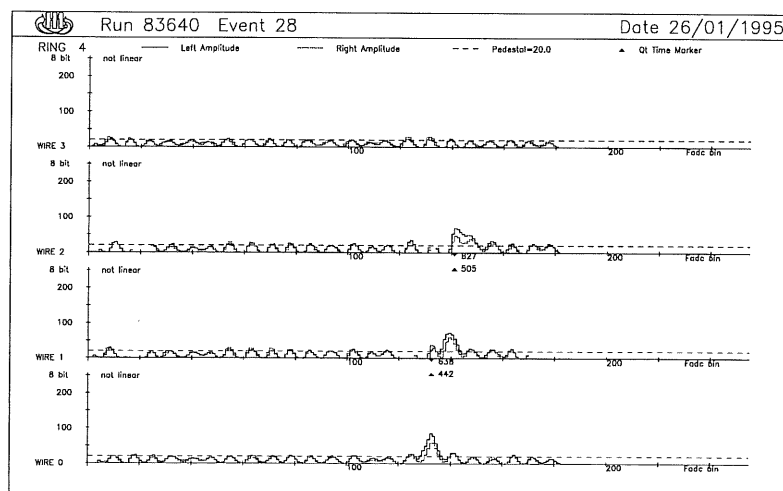


Figure 5.1: In the bottom row is a CIZ-hit, which is not recognized by the charge-time analysis.

Sometimes, pulses which are clearly recognizable in a display of raw FADC information, are not registered by the charge-time analysis. This shows, that

the reconstruction software does not yet make optimal use of the chamber information.

Figure 5.1 shows as an example for such a case the raw data of the CIZ, or more exactly, the digitalised voltage pulses of ring 4. The data from each wire are drawn separately. Note, that the FADC data of both wire ends are superimposed in one diagram. The triangles mark the pulses found.

The pulses of a particle track can be seen on wires 0–2. Wire 3 shows no pulse because the outer wires see particles only on side (section 4.3 and Figure 4.4). We clearly recognize a pulse on wire 0, but the charge-time analysis did not find it because of a software error (counter overflow). This malfunction was identified and corrected using the event shown in Figure 5.1, and resulted in a new version of the Qt -routine [= CIZ- Qt -corr (see section 5.2)].

5.1.2 Time structure

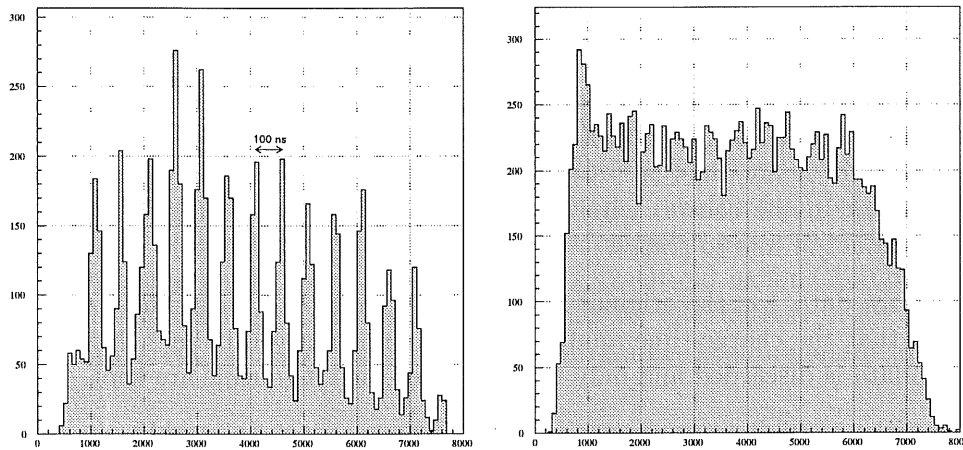


Figure 5.2: CIZ drift time distribution with a 10 MHz structure. On the left side is the condition of summer 94 and on the right side the status of spring 95. The size of the spikes strongly depends on electrical noise conditions in the detector.

The drift time distribution shows a clear 10 MHz structure (compare Figure 5.2). This is due to the 10 MHz noise (see Figure 5.1). By adding this sinusoidal noise to the real pulses, the slope, and therefore the drift time are systematically shifted. In addition, some noise fluctuations are interpreted as real pulses. These faked pulses certainly exhibit the time structure seen in Figure 5.2.

It also has to be taken into account that most pulses in the drift-time-distribution-spikes are not true noise pulses but systematically shifted real pulses, which distorts the z -resolution.

5.2 Comparison between the different charge-time analyses

In the following three different versions of charge-time analysis routines are compared:

CIZ-Qt-old: The original version, used online until summer 94.

CIZ-Qt-corr: A corrected version of CIZ-Qt-old, which does not lose pulses, used online since summer of 94.

COZ-Qt: An adaption of COZ charge-time analysis routine to the special requirements of the CIZ.

5.2.1 The event selection

For this investigation cosmic events are used. In these events a cosmic ray muon passes through the whole detector. In contrast to electron proton events with many different secondary particles, the cosmic muon leaves only one track in the central wire chambers. This prevents ambiguities in the assignment of hits to tracks.

The raw data, i. e. the original FADC data, were stored too in these events, such that the charge-time analysis could be rerun several times. Normally this data is discarded and only the results of the Qt -routine are kept.

To make possible improvements in the efficiency most noticeable, the data were taken with a high voltage lowered to 4100 V as well as with the nominal voltage of 4300 V. The efficiency of the CIZ drops to about 50 % at 4100V.

Each cosmic event used had to meet the following selection criteria:

- There is only one track, i. e. there is no cosmic shower with many particles.
- The track crosses the CIZ twice, so we do not look for non-existing CIZ-hits.
- The distance of closest approach to the center of the beam line is less than 7 cm. With this requirement the tracks cross the CIZ with a large angle in the $r\varphi$ -plane as in the case of electron proton events.

5.2.2 Determination of the efficiency

In order to get a criterion for comparing different Qt -routines, the following procedure is used:

- First, the crossing point of a track in the CJC (central jet chamber) with the CIZ is determined.
- Every CIZ-hit is checked whether it lies within a window $\Delta z = \pm 5$ cm and $\Delta\varphi = \pm 45^\circ$ around this track crossing.
- If a hit is not located near a cosmic track, i. e. not in a track window, it is assessed as a noise hit.
- If a hit within the window is found, it is counted for the efficiency evaluation.
- If more than one hit is found in the window and in the same wire plane, the hits are counted as multiple hits.

The results are displayed in Figures 5.3-5.5.

Every single histogram shows the values determined for different Qt -routines or parameters respectively. The top row shows the efficiency, the middle row the fraction of multiple-hits, and the bottom row the fraction of noise-hits. Each different column refers to a different wire plane. The first bin in each histogram is the value obtained for CIZ-Qt-old or for CIZ-Qt-corr, respectively. The remaining bins are the values for CIZ-Qt-corr or for COZ-Qt for different values of one parameter (for example the minimal integrated charge).

The outer wires (i. e. plane 0 and 3) are much less efficient than the middle ones. This is perfectly reasonable because the outer wires collect only charge from one side (see section 4.3). Still the efficiency is higher than half of the inner wires, because some noise hits are interpreted falsely.

For each parameter of the COZ-Qt these plots were made to find the optimal value. Only the plots for the integration length are shown, for reasons of space, and because the efficiency only weakly depends on many parameters.

In Figure 5.3 the CIZ-Qt-old is compared with the CIZ-Qt-corr. The efficiency increases because the CIZ-Qt-corr does not miss hits like the one shown in Figure 5.1. The plots show the effect is larger in the inner wires, even though the error had been discovered for an outer wire,

The charge-integration length is varied from 3 to 10 FADC bins in Figures 5.4 and 5.5. In the lower voltage data the efficiency increases up to an integration length of 7 bins and then remains constant. At the nominal voltage no significant dependence on the integration length can be observed.

The use of the COZ- Qt code shows no noteworthy improvement of the efficiency over the CIZ- Qt code. Therefore it is not possible to reduce the high-voltage of the CIZ using the COZ- Qt .

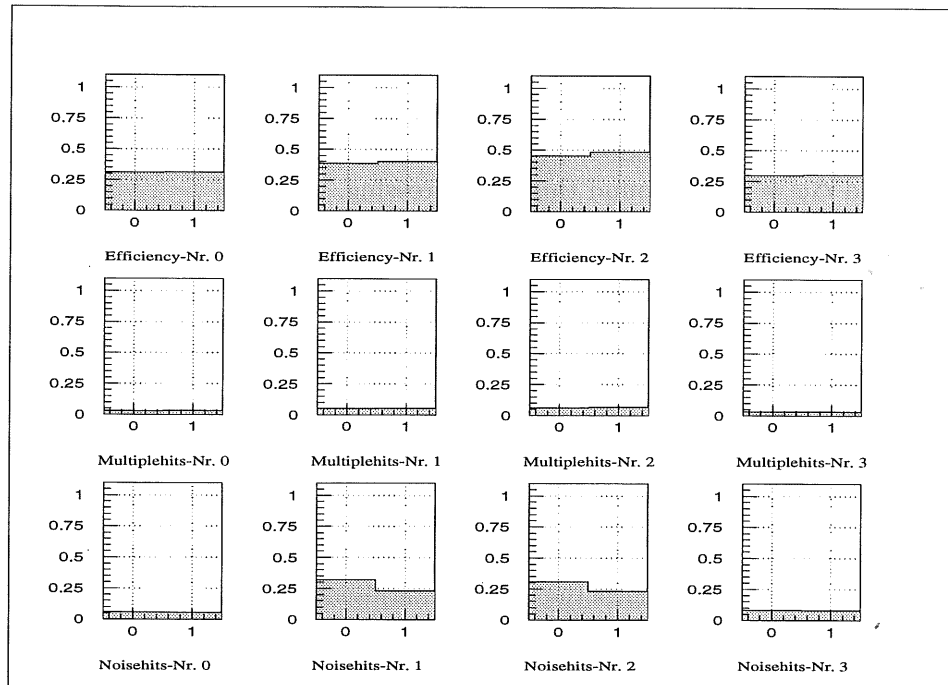


Figure 5.3: Comparison of the CIZ- Qt -old (histogram bin 0) with the CIZ- Qt -corr (histogram bin 1). The high voltage was reduced to 4100 V, which leads to a lower efficiency of about 50% and therefore to larger effects in the efficiency improvement. See section 5.2.2 for a detailed explanation of this plot.

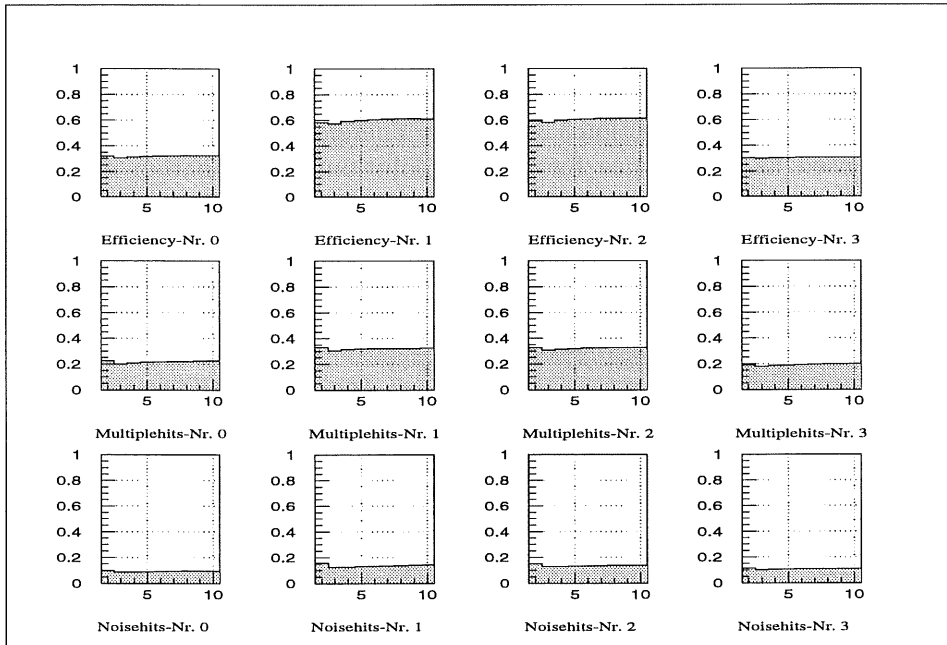


Figure 5.4: Comparison of the CIZ- Qt -corr (histogram bin 2) with the COZ- Qt (histogram bin 3-10) (Bin Number = number of FADC bins over which the pulse was integrated for the charge determination) [high voltage: 4300 V = nominal value].

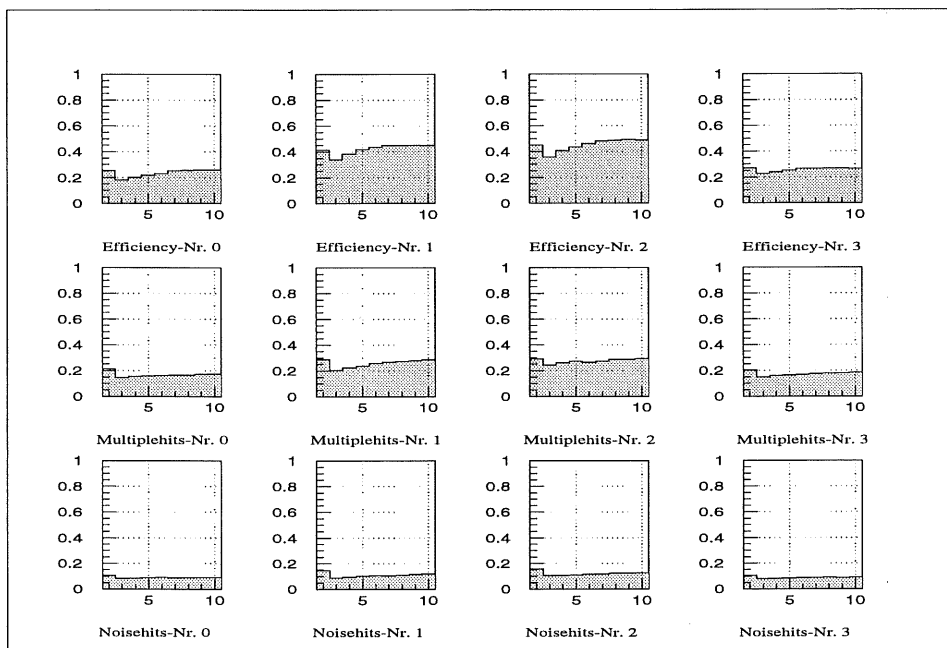


Figure 5.5: Comparison of the CIZ- Qt -corr (histogram bin 2) with the COZ- Qt (histogram bin 3-10) [high voltage reduced to 4100 V].

5.2.3 Comparison of the φ -resolution

The track- φ -coordinate is much better measured by the jet-chambers than by the z -chambers (see section 3.3 and 4.4). Therefore, the CJC- φ -coordinate can be used as a reference for the φ -resolution determination of the z -chambers, in particularly the CIZ.

For every hit the φ -difference between the CIZ and the nearest CJC-track is computed (see Figure 5.6). The nearest track is the one with the smallest chi-squared $\left(\chi^2 = \left(\frac{\Delta\varphi}{\sigma_\varphi}\right)^2 + \left(\frac{\Delta z}{\sigma_z}\right)^2\right)$.

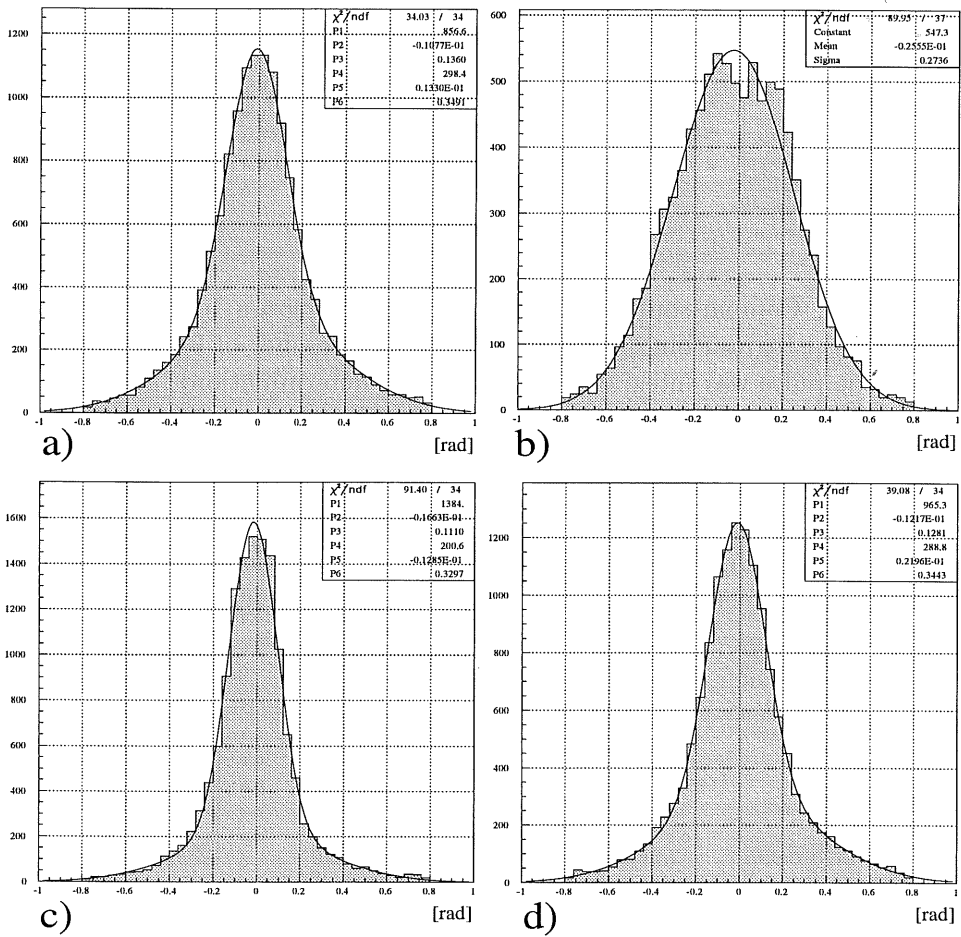


Figure 5.6: φ -resolution of the CIZ- (a) and COZ-Qt (b,c,d). The resolution of the COZ-Qt is plotted for three different integration length [0 bins (b), 7 bins (c), d: 28 bins (d)]. The numbers in the upper right corner show the results of the Gaussian fits (see text for a detailed description).

For suppression of noise hits $\Delta z (= z_{hit} - z_{track})$ of less than 10 cm is required.

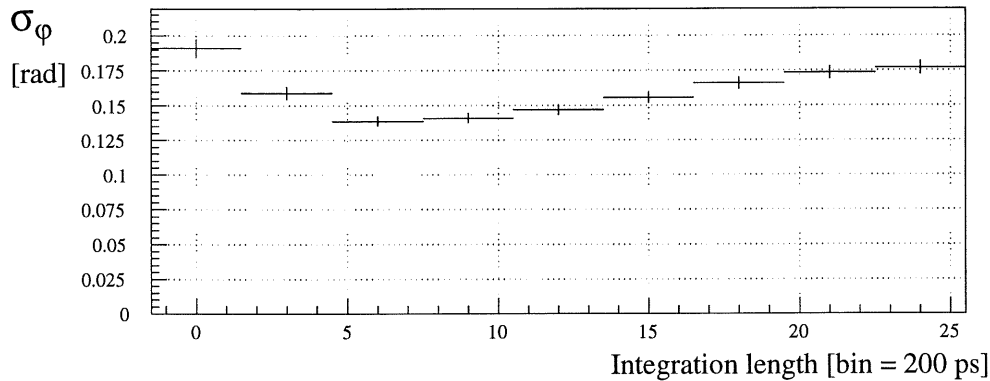


Figure 5.7: φ -resolution versus charge integration length of the COZ-Qt code. The first bin shows the φ -resolution for the CIZ-Qt code. The error of σ_φ is computed from errors of fit-parameters and the horizontal bars indicate the bin width.

To determine the resolution, two Gaussian distributions were fitted to the histograms in Figure 5.6.

$$f(x) = P_1 \cdot e^{-\frac{(x-P_2)^2}{P_3^2}} + P_4 \cdot e^{-\frac{(x-P_5)^2}{P_6^2}} \quad (5.1)$$

The first one, higher and narrower, should describe the good hits. The second one, wider and smaller, represents noise hits and hits where the charge determination failed, because of secondary hits or a superposition with exceptionally large noise.

The two summands of $f(x)$ show a rather strong correlation in the fit. Therefore the width is defined as the weighted average of parameters P_3 and P_6 [from Figure 5.6], i. e. of the width of the two Gaussian distributions.

$$\sigma_\varphi = \frac{P_3 \cdot P_1 + P_6 \cdot P_4}{P_1 + P_4} \quad (5.2)$$

In Figure 5.7 the width of the φ -resolution is plotted versus the charge-integration-length of the COZ-Qt. The first bin shows the φ -resolution-width of the CIZ-Qt-old. We observe that a longer integration-length increases the width of the φ -distributions.

Therefore the φ -resolution of the CIZ-Qt is worse, because the CIZ-Qt integrates over the whole pulse and not just over the first few bins. The optimal integration length is around 7 bins. A value, which shows also optimal behavior in the efficiencies (see Figure 5.5).

5.2.4 Comparison of the z -resolution

The φ -resolution depends directly on the accuracy of the charge determination. In contrast to that, many different factors influence the z -resolution (see 4.4):

- The accurate measurement of the drift time, and therefore of the Qt -analysis.
- The calibration of the drift velocity and the time constant t_0
- The exact description of the isochrones, i. e. a suitable parameterization of the isochrone map.

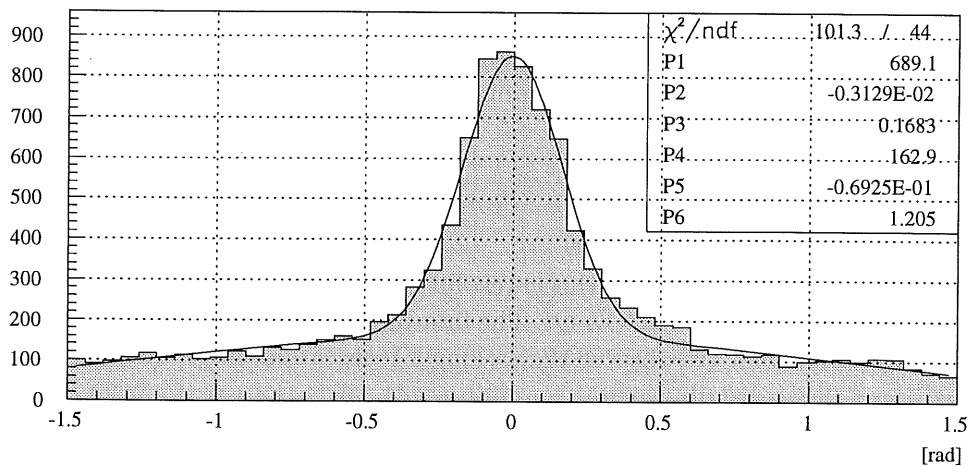
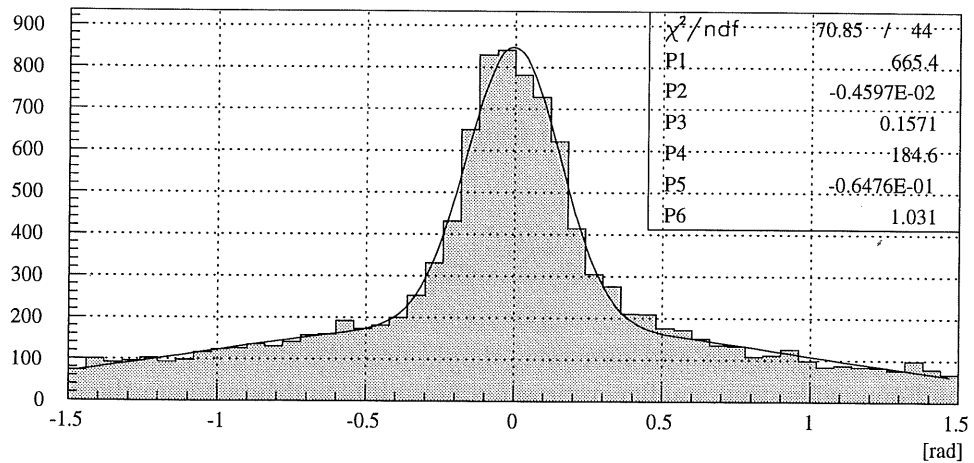


Figure 5.8: z -resolution ($z_{hit} - z_{track}$) of the CIZ- and COZ- Qt without a separate calibration for each Qt -routine.

For an accurate comparison of the z -resolution of the two Qt -routines, a separate calibration for each Qt -routine has to be done first. Additionally, for an accurate z -resolution determination, the event selection cuts would be harder: for example minimal two or three COZ-hits for each track would be required. This has not been done in this analysis, because of statistical reasons.

Therefore, the two plots Figure 5.8 do not show yet the best possible z -resolution of the CIZ, which has to be determined in a further analysis. At this stage, none of the two routines shows a significantly better resolution.

5.3 Conclusions

Table 5.1: Comparison of the CIZ- with the COZ-charge-time-analysis with optimized parameters. The performance of the COZ- Qt is in every single point slightly better.

	Efficiency		Multiple-hits		Noise-hits	
	Outer Wires	Inner Wires	Outer Wires	Inner Wires	Outer Wires	Inner Wires
CIZ- Qt	31.1%	58.8%	20.9%	32.8%	10.5%	15.3%
COZ- Qt	31.3%	61.1%	20.8%	32.4%	10.0%	13.5%

The performance of both charge-time-analysis-routines are about the same. Therefore, we are not forced to switch the Qt -routines. Nevertheless, the COZ- Qt performance is in every single point better. The efficiency is about 1% higher, whereas the multiple- and noise-hits remain low or even slightly decrease.

The main improvement could however be achieved in the φ -resolution, where, by using the COZ- Qt with 7 bins integration length, a reduction of about 27% of φ uncertainty is observed.

In case of switching the Qt -routines, a new calibration of the drift-velocity and mainly of the time-constant t_0 has to be done. The final decision can be taken only after a comparison of the two *separately* calibrated charge-time-routines.

Chapter 6

Investigations pertaining to the ϑ -resolution

6.1 Introduction

By determining the kinematic variables with the electron-only method, the electron scattering angle ϑ and therefore the z -chambers are of crucial importance (see section 2.3).

The polar angle covered by the CIZ and COZ are $16^\circ < \vartheta < 169^\circ$ and $25^\circ < \vartheta < 156^\circ$, respectively. If the electron is scattered into this angular region, Q^2 is high (see equation (2.5)). Thus, a sample of high Q^2 events was used for the following investigation on the ϑ -resolution.

From the intrinsic resolution of the z -chambers (CIZ 0.26 mm, COZ 0.20 mm) and the radial distance between CIZ and COZ (286 mm, see [6] Table 4.2) we expect an optimal angular resolution of

$$\frac{\sqrt{(0.26)^2 + (0.20)^2}}{286} = 1.1 \text{ mrad} . \quad (6.1)$$

This value could be improved by making use of two or three hits per z -chamber and the z -vertex, which is determined by many tracks as well.

Our study was done with simulated events and real electron-proton data. For the former the elementary interaction between the electron and proton is generated by Monte-Carlo methods and the whole detector response is simulated in every detail. The big advantage is that one knows the 'real' process, not only the detector response, i. e. we have access to every basic quantity of the event.

In our case, these are the kinematic variables or, more exactly, the electron energy and scattering angle. These reference values can be compared

with the ‘measured’ quantities. In Monte-Carlo generated events, ‘measured’ quantities are derived from the simulated detector responses. Additionally one can check the fraction of particles, which were identified falsely as an electron.

But simulated events are not the reality. One has to crosscheck whether the simulation is in agreement with the real data or not. The easiest method to do that is to compare the distribution of corresponding quantities in data and simulation.

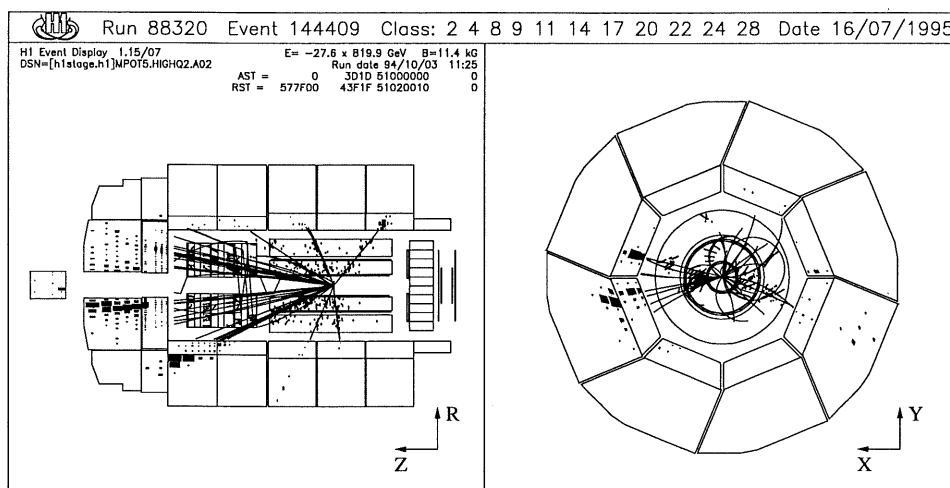


Figure 6.1: A typical high- Q^2 -event. One can easily recognize the scattered electron in the upper right part of the detector (rz -view) and on the left side in the xy -view. It deposits its energy only in the electromagnetic part of the calorimeter, in contrast to the hadrons on the lower left side (rz -view).

For example there are several different possibilities to deduce the electron scattering angle ϑ :

- Use directly the polar angle of generated scattered electron ($= \vartheta_{Gen}$) (only in Monte-Carlo generated events)
- Use data from the central jet chamber alone ($= \vartheta_{CJC}$) to reconstruct the scattering angle.
- Use the CJC in combination with one or both z -chambers (CIZ and COZ) ($= \vartheta_{CIZ}, \vartheta_{COZ}, \vartheta_Z$) to determine ϑ more accurately.
- Use the center of gravity of the deposited energy cluster in the calorimeter ($= \vartheta_{Clu}$)

In all but the first method the z -event vertex [derived from the all the tracks of the event] is used as one relatively accurate z -coordinate of the track. This

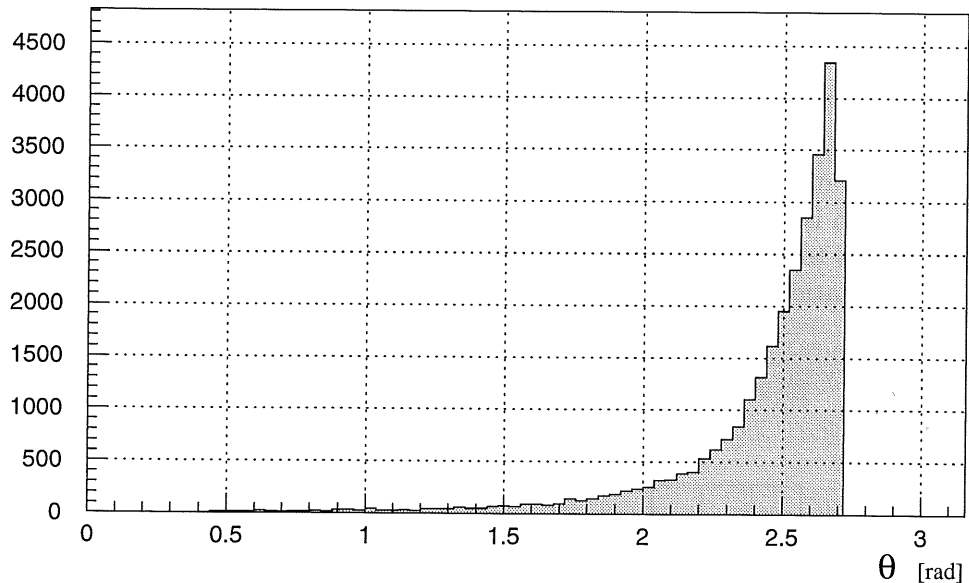


Figure 6.2: ϑ -distribution of the simulated event-sample.

has consequences, as are shown in section 6.4, if the vertex is determined wrongly.

For simulated events the exact scattering angle (ϑ_{Gen}) is known. Therefore, it is possible to determine the resolution for every different method of ϑ determination ($\vartheta_{...} - \vartheta_{Gen}$). Figure 6.2 shows the distribution of the generated scattering angles.

In real electron-proton events, ϑ_{Gen} is not available. The only possibility to check the ϑ -resolution is to compare the different ϑ with each other. As ϑ_Z is the most accurate, it can be used quasi as reference angle. These resolutions ($\vartheta_{...} - \vartheta_Z$) can be determined with data and Monte-Carlo events. So they are used to check the correctness of the simulation of our detector.

6.2 Data processing

6.2.1 Event selection

As already mentioned, a high Q^2 data and simulated event sample was used as a base selection. Additionally, the events had to fulfill the following conditions:

- The energy of the scattered electron had to be larger than 7 GeV, to suppress background (for example a pion falsely identified as an electron).

- The electron scattering angle had to fall into the angular acceptance of the CIZ and COZ ($25^\circ \leq \vartheta \leq 156^\circ$).

6.2.2 The different version of deducing the scattering angle ϑ

For a better understanding of the different possibilities to determine electron scattering angle ϑ , we include a very short introduction to the track reconstruction. A description in greater detail can be found in [10].

- In the first step helix curves are fitted to the CJC-data of the particle tracks.
- The formerly independent tracks are then constrained to a common event vertex for improving the z -resolution. Tracks, for which this is not possible, i.e. the χ^2 gets too large, are linked to secondary vertices.
- In the third step the vertex constrained tracks are linked to the z -chamber-data for getting the best possible z -resolution. Simultaneously the z -coordinate of the event vertex is improved.

ϑ_{Gen} : comes directly from the simulated data.

ϑ_{CJC} : is extracted out of the vertex constrained CJC-tracks.

ϑ_Z : Deducing the scattering angle out of the z -linked tracks, one gets the most accurate ϑ .

ϑ_{CIZ} : For linking the CJC-tracks to the z -chamber information, the COZ hits in a window ($\Delta z = \pm 3.5 * \sigma_{z_{CJC}}, \Delta \varphi = \pm 3.5 * \sigma_{\varphi_{COZ}}$) around the electron track are ignored. The remaining hits are still used for linking of all other tracks, which preserves the high accuracy of the vertex in z -direction. This method allows us to study the influence of the CIZ onto the ϑ_Z -resolution.

ϑ_{COZ} : is the same as ϑ_{CIZ} , but rather than ignoring COZ hits, the CIZ hits around the electron track remain unused.

ϑ_{Clu} : One point is determined by the center of gravity of the deposited energy in the calorimeter, and the other is obtained from the event vertex (improved by the z -linked tracks).

6.3 ϑ -resolution in data and simulation

Figure 6.3 shows the ϑ -resolution deduced from the simulations, i. e. in every histogram $\vartheta_{\dots} - \vartheta_{Gen}$ is plotted. To determine the resolution, again two Gauss-distributions were fitted to the data.

$$f(x) = P_1 \cdot e^{-\frac{(x-P_2)^2}{P_3^2}} + P_4 \cdot e^{-\frac{(x-P_5)^2}{P_6^2}} \quad (6.2)$$

The first one, higher and narrower, fits to the peak, the wider and smaller one represents the non-Gaussian-tails. These tails are discussed in section 6.4.

- ϑ_Z : It has a resolution of about 0.6 mrad. This is by far the best one. The tails result from events with a badly reconstructed z -vertex, as shown in section 6.4.
- ϑ_{CIZ} : Its resolution is relatively bad ($\sigma_{z_{CIZ}} \approx 5$ mrad) because of the short distance between the event vertex and the CIZ. However, the CIZ is important for the determination of the scattering angle, because without the CIZ, an accurate measurement of the event vertex z -position would not be possible. The vertex z -position is used in nearly all methods of the ϑ -determination.
- ϑ_{COZ} : It almost reaches the ϑ_Z -resolution but it indirectly profits from the CIZ via the accurate vertex as already mentioned above.
- ϑ_{Cu} : With about 2.6 mrad, the resolution is about four times worse than the one of ϑ_Z . Note that there is a systematic shift of the same order of magnitude (2.5 mrad). This indicates, that the relative alignment of the calorimeter and the tracking system is not correct yet.
- ϑ_J : It has by far the worst resolution, about ten times wider than the one of ϑ_Z , which is expected from the z -resolution of the CJC of about 3 cm.

Figure 6.4 compares data with Monte-Carlo events. On the left side are the simulated distributions and on the right side the real measured events. The plots show that the Monte-Carlo simulation describes the tracking too optimistic.

First of all, there's a small systematic shift of about 1 mrad between Monte-Carlo generated events and data in the case of $\vartheta_{CIZ} - \vartheta_Z$, $\vartheta_{CIZ} - \vartheta_{COZ}$ but much less in $\vartheta_{COZ} - \vartheta_Z$. A further shift of about 2.2 mrad can be observed in the $\vartheta_J - \vartheta_Z$ distribution. A wrong relative position of the CIZ and COZ would not result in a systematic shift of $\vartheta_Z - \vartheta_{CIZ}$. However an incorrectly

calibrated z -position of the CJC relative to the z -chambers can explain both systematic shifts. ϑ_{CIZ} is more strongly influenced by the CJC-track than ϑ_{COZ} or ϑ_Z , because of the much shorter lever arm between the vertex and the CIZ than between the vertex and the COZ.

Additionally all the resolution curves are about 50% wider in the data compared to the simulation. However the cluster method is very well described by the simulation. Only the systematic shift of ϑ_{Clu} compared to ϑ_Z differs slightly.

The angular dependence of the ϑ -resolution (see Figure 6.6) for the simulation agrees with the real data. As already observed above, the resolution width is simulated too small.

The simple geometrical estimation of the $\sigma_{\vartheta_{COZ}}$ for $\vartheta = \frac{\pi}{2}$ (radius of the COZ = 472 mm)

$$\sigma_{\vartheta_{COZ}} = \frac{\sqrt{(0.2mm)^2 + (1.3mm)^2}}{472mm} = 2.8 \text{ mrad} \quad (6.3)$$

is more than a factor of two larger than the value determined in this analysis with simulated events (= 1.3 mrad) (see Figure 6.3 d). But we have to take into account that most events in this high Q^2 sample have a ϑ around 2.6 rad (see Figure 6.2). Therefore σ_{ϑ} of this analysis is actually $\sigma_{\vartheta}(\vartheta \simeq 2.6)$

As Figure 6.6 shows $\sigma_{\vartheta}(\vartheta = \frac{\pi}{2})$ is about a factor of two larger than the $\sigma_{\vartheta}(\vartheta = 2.7)$, because at this angle the lever arm between the vertex and the COZ becomes much bigger and because $\sigma_{\perp Vertex}$ (=projection of σ_{Vertex} in the direction of the scattered electron) decreases with a factor of $\sin \vartheta$ ($\sigma_{\perp Vertex} \simeq \sin \vartheta \cdot \sigma_{zVertex} \ll \sigma_{zVertex} \gg \sigma_{xyVertex}$, $\sigma_{zVertex} \simeq 1.2 \text{ mm}$ (see Figure 6.10 c), $\sigma_{xyVertex} \simeq 0.17 \text{ mm}$ (see [6])).

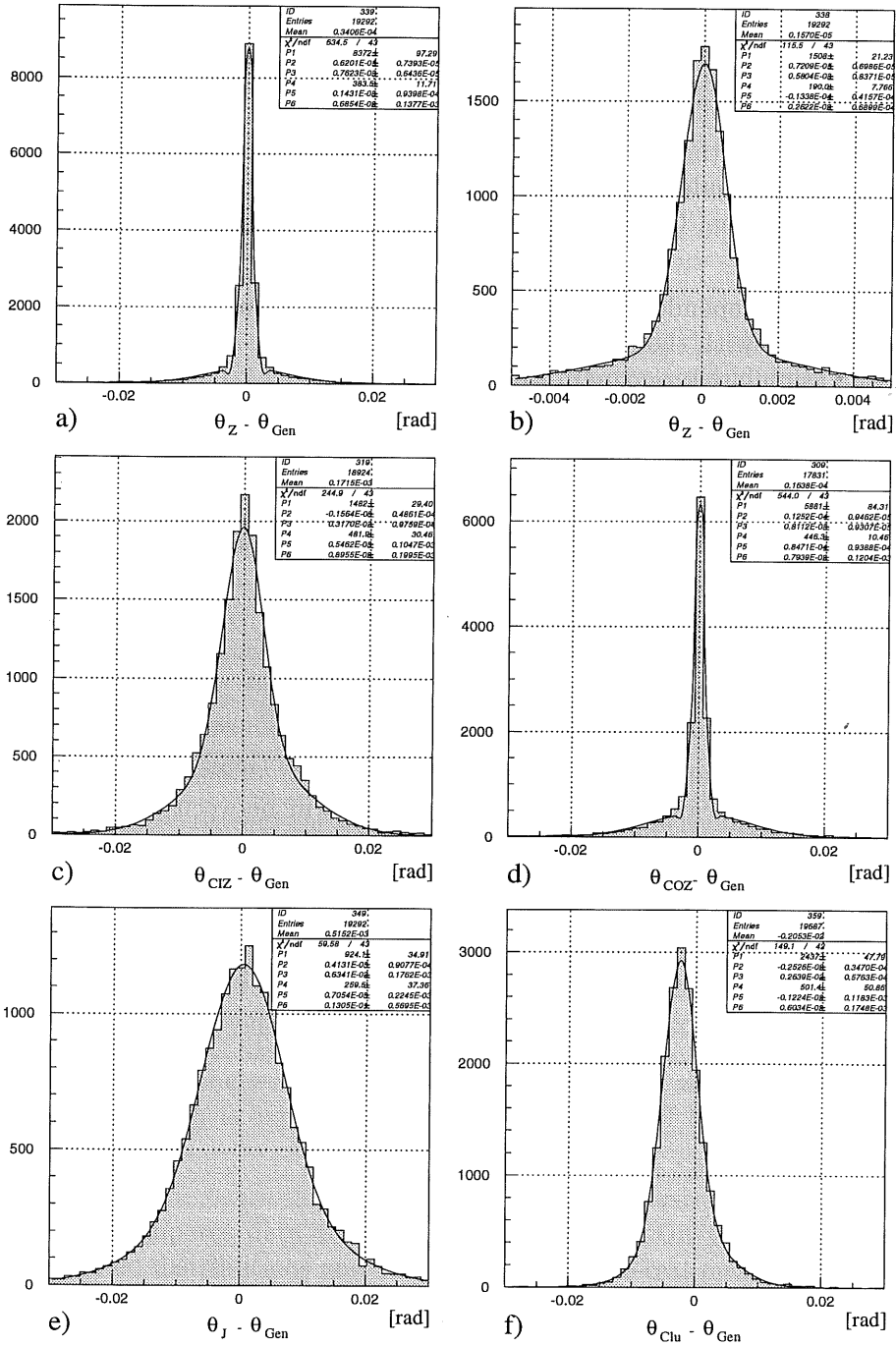


Figure 6.3: ϑ -resolution obtained from Monte-Carlo simulation for different methods of determining the electron scattering angle ϑ . The function fitted to the data is defined in Formula (6.2).

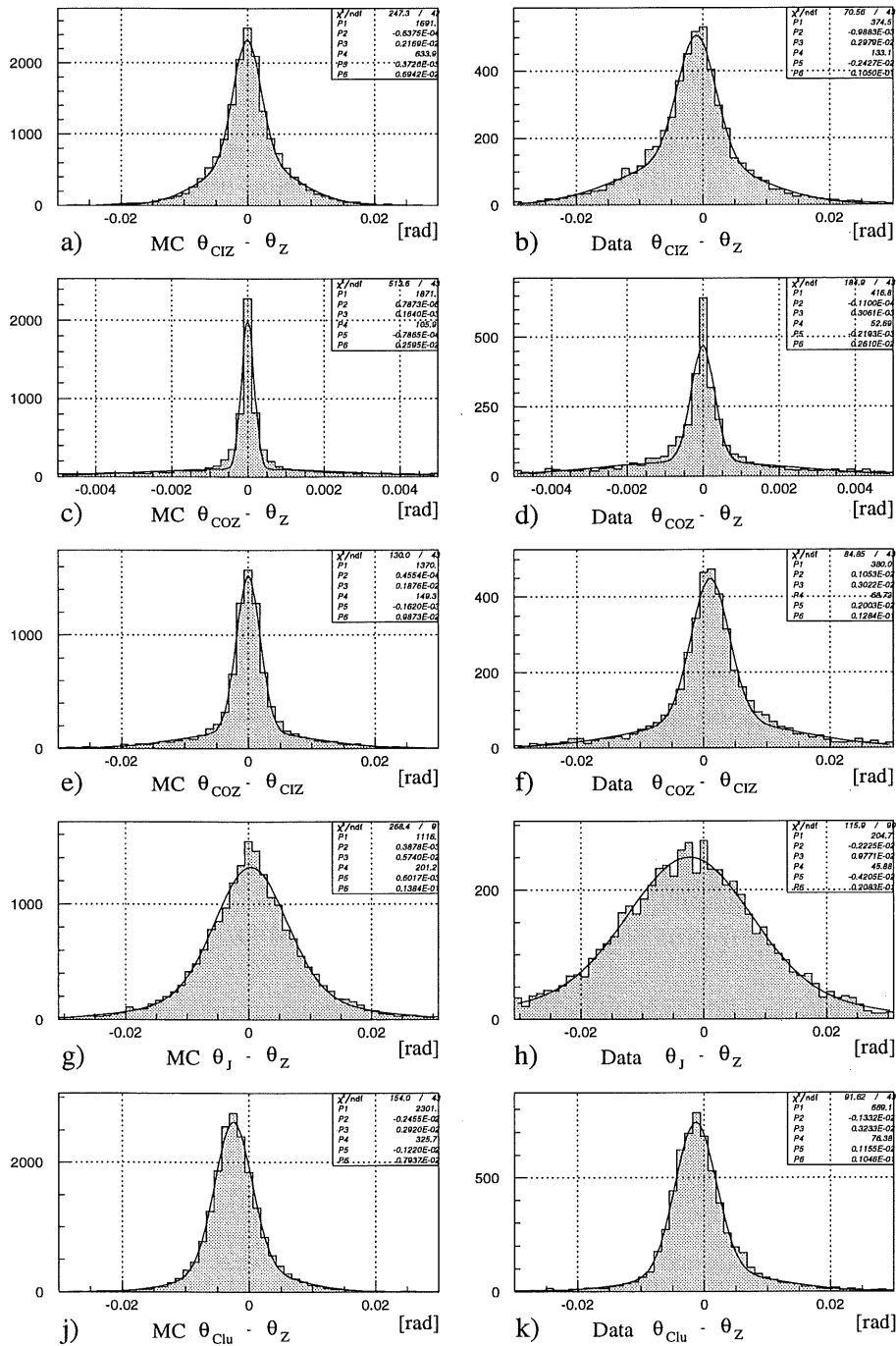


Figure 6.4: Comparison between the simulated and the real ϑ -resolution. On the left side the Monte-Carlo distributions are shown and on the right side, real data.

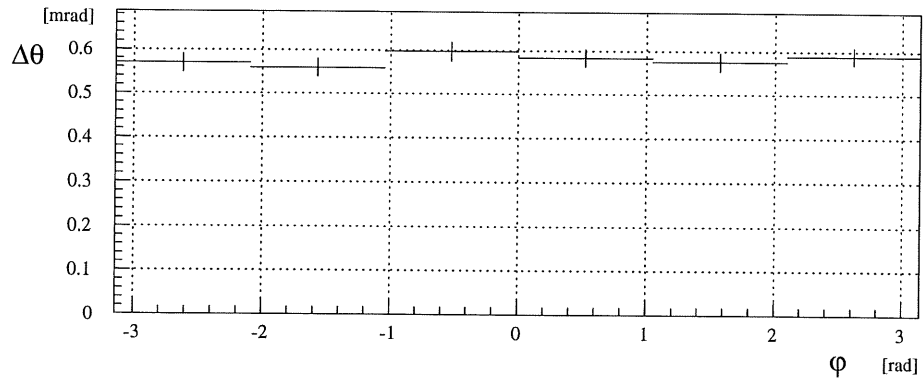


Figure 6.5: ϑ -resolution versus φ . As expected there's no φ -dependency.

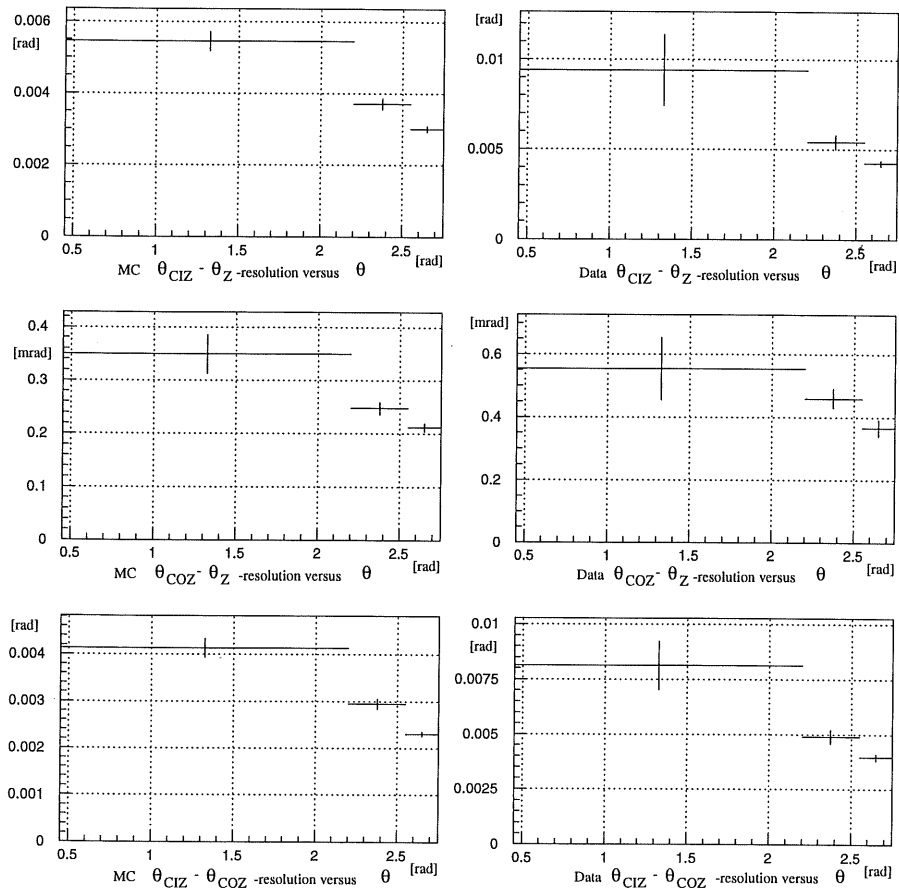


Figure 6.6: ϑ -resolution versus ϑ . Though the absolute values disagree between data and Monte-Carlo the observed angular dependence is as expected.

6.4 Non-Gaussian tails in the ϑ -resolution

The resolution of ϑ_Z shows non-Gaussian tails, i. e. it cannot be described by a single Gauss distribution. Therefore further investigations are necessary to understand the reason. In a second step one can try to eliminate or at least suppress these tails.

The left column of Figure 6.7–6.9 show various distributions without any cuts. The events in the middle column are selected to lie in the center of the distribution ($|\Delta\vartheta_Z| < 0.003$). And in the right column they are restricted to the tails $|\Delta\vartheta_Z| \geq 0.003$.

The top row shows $\Delta\vartheta_Z \equiv \vartheta_Z - \vartheta_{Gen}$. In the second row $\frac{1}{\sigma_{zVer}}$ is plotted for the different cuts. σ_{zVer} is the estimated error of the z -position of the vertex. It is calculated during the event reconstruction in the track fit procedure. The same histograms are plotted again in the third row, but normalized to the first histogram in the second row:

$$\text{histogram h)} = \frac{\text{histogram e)}}{\text{histogram d)}} \quad (6.4)$$

The following rows refer to the same as what is plotted for $\frac{1}{\sigma_{zVer}}$, but they show other possible relevant quantities. These are the number of linked Z-, CIZ- and COZ-hits and the electron energy.

The σ_{zVer} shows a significantly different distribution for $|\Delta\vartheta_Z| < 0.003$ and for $|\Delta\vartheta_Z| \geq 0.003$ (see Figure 6.7 d–f). About ten percent of the events with a small σ_{zVer} ($\sigma_{zVer} < 0.33$) contribute to the tails. Therefore one can cut at about $\sigma_{zVer} = 0.33$ to separate events with a wide $\Delta\vartheta_Z$ from events with a narrow one.

As the plots (k–m) in the fourth row of Figure 6.7 show, many events in the tails do not have any z -hits linked. It is obvious, that these events cannot have a good ϑ_Z -resolution. In Figure 6.8 these distribution are broken down according to number of linked CIZ- and COZ-hits, respectively. Events in the middle column have a small $\Delta\vartheta_Z$, therefore they need accurate z -points, that is to say COZ-hits (see histogram l). CIZ-hits are not as necessary because of the shorter leverage (see histogram e).

The third column is even more interesting. Most events in the tails do not have any CIZ-hits linked (see histogram f). This is probably not because the CIZ is not efficient, but due to a wrong z -vertex determination. For linking CIZ-hits, the vertex has to be relatively accurate in contrast to linking COZ-hits, where even with a badly reconstructed vertex the tracks can be bent to catch the hits (see histogram p). If the only reason for not linked hits would be the efficiency of the CIZ, the distribution of histogram f would look like a binomial distribution and it does not.

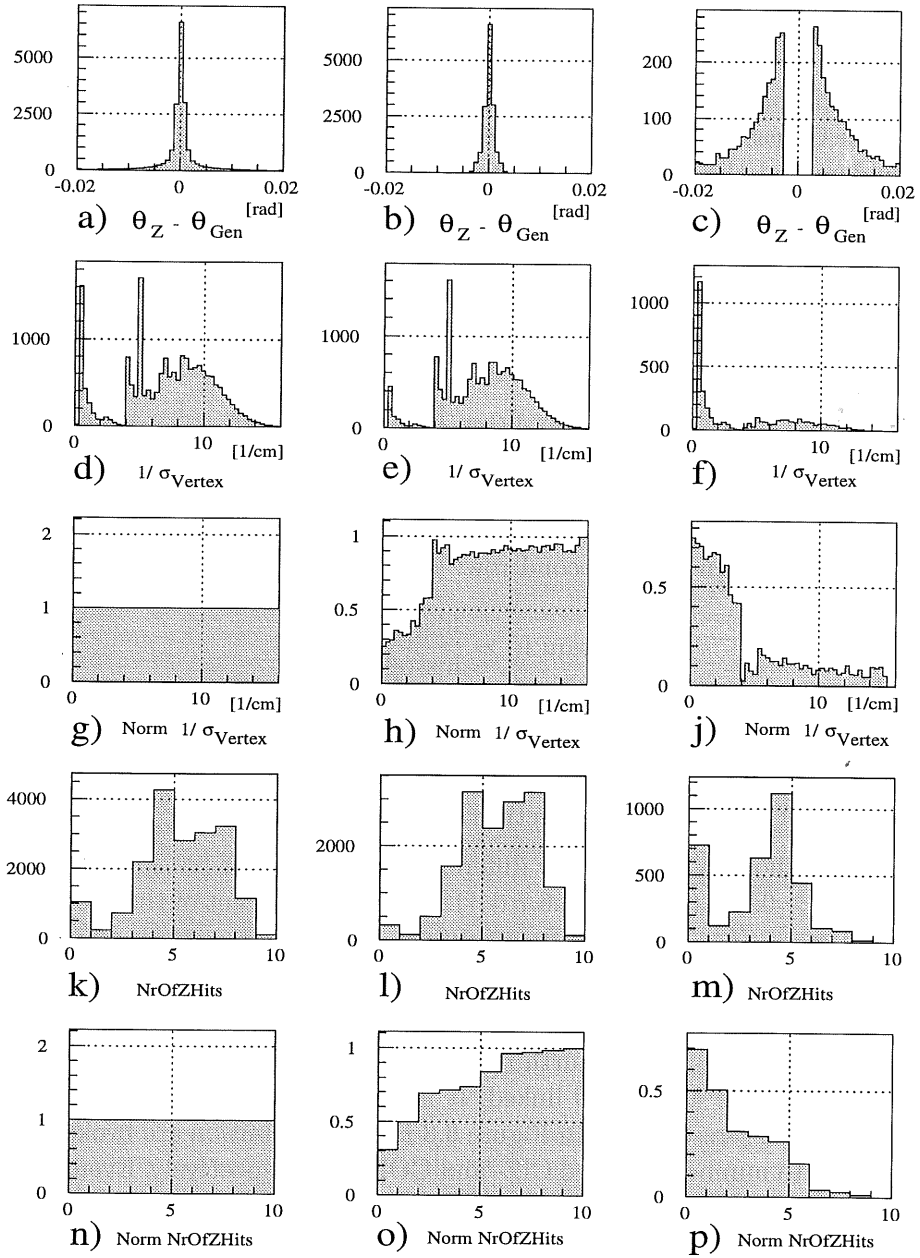


Figure 6.7: Comparison of the distribution of $\frac{1}{\sigma_{zVert}}$ and number-of-Z-hits with respect to a cut ' $\Delta\theta < 0.003$ '.

left column: all events
middle column: events remaining after cut
right column: events rejected by cut

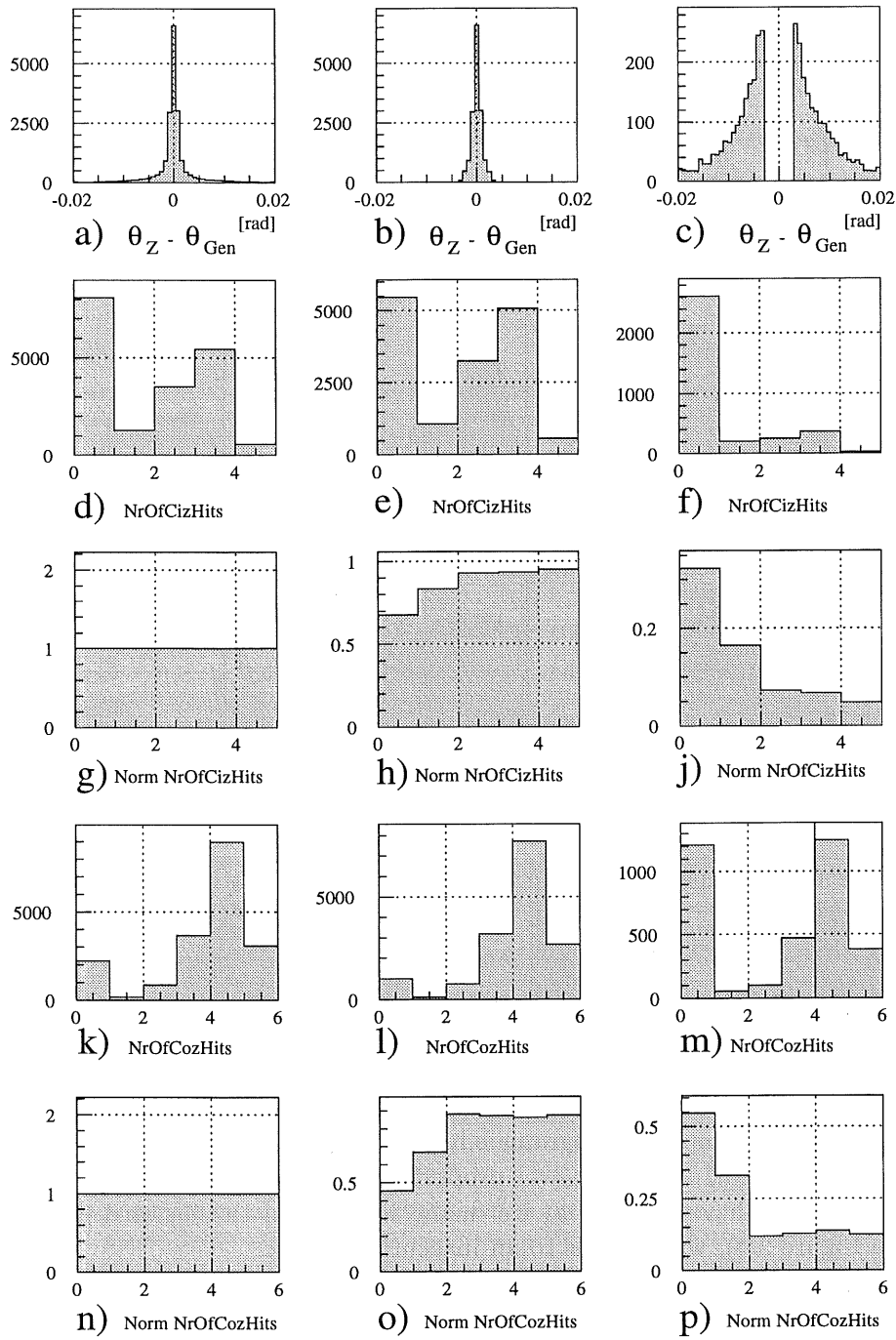


Figure 6.8: Comparison of the distribution of number-of-CIZ-hits and number-of-COZ-hits with respect to a cut ' $\Delta\theta < 0.003$ '

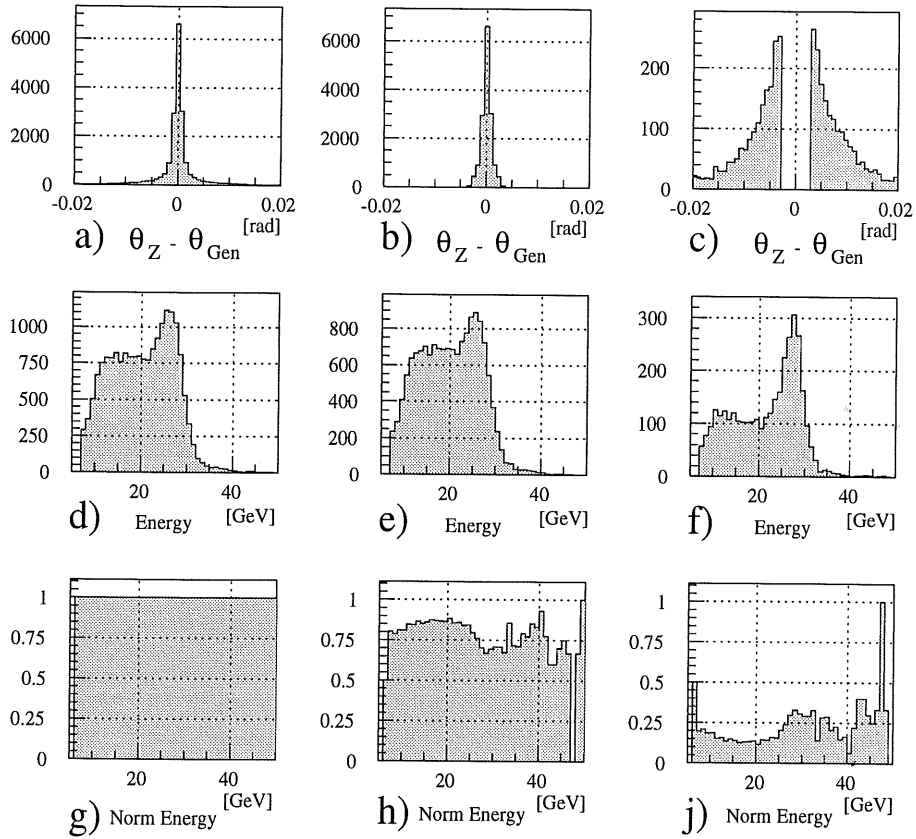


Figure 6.9: Comparison of the energy distribution with respect to a cut ' $\Delta \vartheta < 0.003$ '

As Figure 6.9 shows, the electron energy is not strongly correlated with the ϑ -resolution (compare histograms e,h with f,j). Nevertheless, events in the kinematical peak contribute over proportional to the tails (see histogram j). These events have a larger x , i.e. many hadrons in the forward direction (see Figure 2.4), which leads to an inaccurate vertex.

Figure 6.10 shows the ϑ -distribution with the proposed cuts ($\sigma_{zVer} < 0.33$ or $\sigma_{zVer} \geq 0.33$) applied to. The non-Gaussian-tails are suppressed by a factor of four by this cut (see plots g and h). The rejected events have a $\sigma_{\vartheta Z}$ of about 8.3 mrad (see histogram f), which is about the same as $\sigma_{\vartheta J}$ and corresponds nicely to the width of the tail in Figure 6.3 histogram a and b as expected.

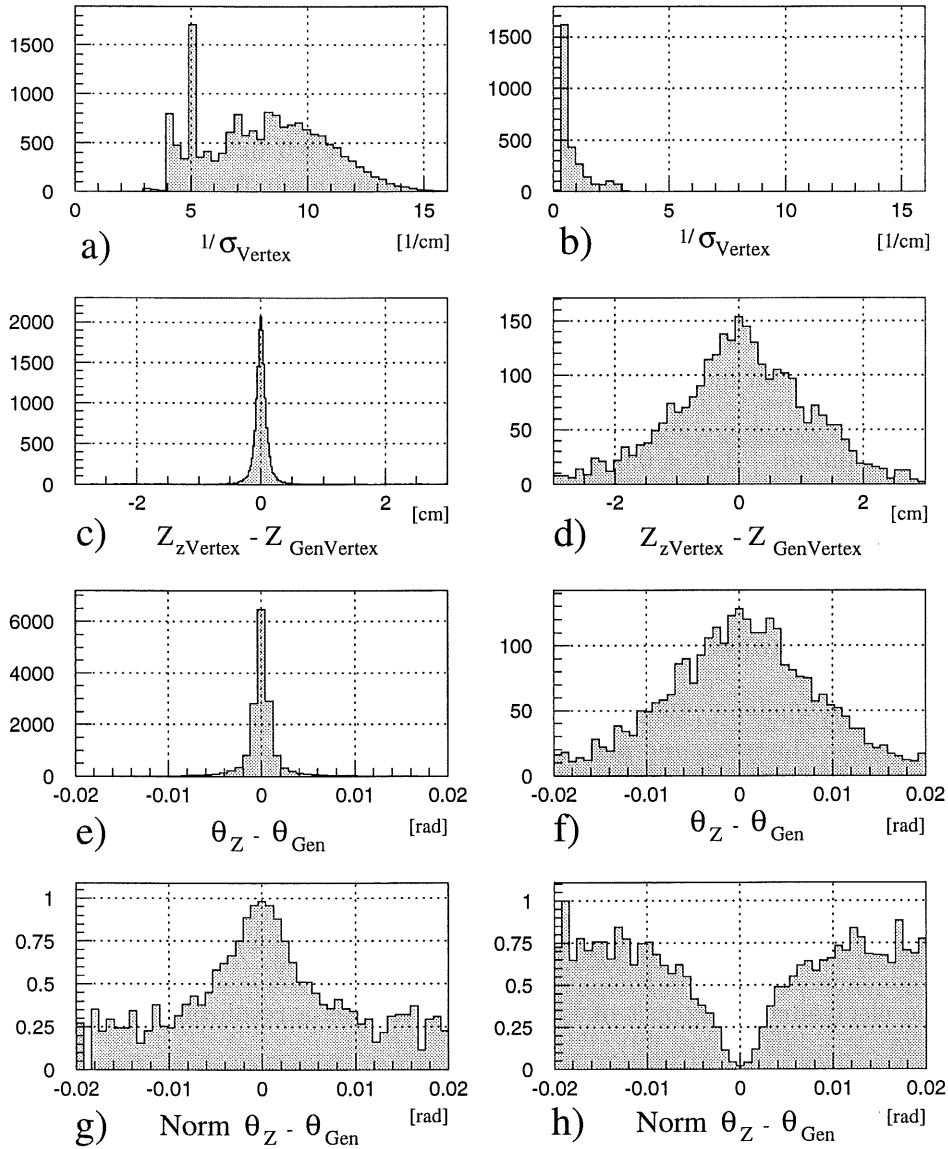


Figure 6.10: ϑ -resolution with respect to a cut ' $\sigma_{zVertex} < 0.33$ '. At the bottom, the acceptance of the cut versus $\Delta\vartheta$ is plotted.

The events with $4.5 \frac{1}{[cm]} \leq \frac{1}{\sigma_{zVertex}} \leq 5.5 \frac{1}{[cm]}$ (see Figure 6.10, histogram a) were studied separately and did not show any worse z_{Vertex} -resolution than the average event (histogram c). However the events with $\frac{1}{\sigma_{zVertex}} \leq 3.3 \frac{1}{[cm]}$ have not used any z -chamber information and have therefore a z_{Vertex} -resolution comparable to the CJC alone (see histogram d).

6.5 Conclusions

Measuring electron scattering angle with the z -linked track rather than with the energy cluster position, one gains a factor of 3.5 in accuracy. The efficiency remains high (see Table 6.1). By requiring a small error in the vertex determination one can reduce the tails of the ϑ -measurement by a factor of four, but loses 16% of efficiency.

Table 6.1: Comparison of ϑ -resolution for the different ϑ -determination methods.

	ϑ_Z	$\vartheta_Z (\sigma_{zVer} < 0.33)$	ϑ_{clu}	ϑ_J
σ_ϑ [mrad]	0.91 ± 0.02	0.80 ± 0.02	3.2 ± 0.1	7.9 ± 0.3
efficiency	98.0 %	82.6 %	100 %	98.0 %

6.5.1 Estimation of the errors of x and Q^2

As already shown in section 2.3, the errors of kinematic variables x and Q^2 depend on the measured quantities the following way:

$$\frac{\delta Q^2}{Q^2} = \sqrt{\left(\frac{dE'}{E'}\right)^2 + \left(\tan \frac{\vartheta}{2} d\vartheta\right)^2}$$

$$\frac{\delta x}{x} = \sqrt{\left(\frac{1}{y} \frac{dE'}{E'}\right)^2 + \left(\tan \frac{\vartheta}{2} \left(x \frac{E_p}{E_e} - 1\right) d\vartheta\right)^2}$$

The electromagnetic part of LAr-calorimeter has a resolution of the order of $\frac{\delta E}{E} = \frac{12\%}{\sqrt{E [GeV]}}$ (see [6]).

The simulation of the detector is not yet as good as desired. The ϑ -resolution is about 30 % too narrow. Additionally, I have found a tracker alignment problem: Most probably the relative position of the CJC to z -chambers is wrongly calibrated.

The estimated relative errors for two particular events have been calculated in Table 6.2. The first event was chosen for showing a large $d\vartheta$ -dependency of $\frac{\delta Q^2}{Q^2}$. The second event has one of the highest ever measured Q^2 . Therefore its $\frac{\delta x}{x}$ depends as much as possible on $d\vartheta$.

With the determination of ϑ by tracks using the z -chamber information, we have reached an adequate performance. Further optimization is not necessary at this moment, because the errors of the kinematic variables will be dominated by the energy error (see Table 6.2).

Table 6.2: Estimated errors of x and Q^2 for two particular events: the first one lies in the kinematic peak and the second one has an extremely high Q^2 .

	$\vartheta_{Clu} : \frac{\delta Q^2}{Q^2}$	$\vartheta_Z : \frac{\delta Q^2}{Q^2}$
$E = 25 \text{ GeV}$ $\vartheta = 156^\circ$ $Q^2 = 117 \text{ GeV}^2$ $x = 0.012$	$\sqrt{(2.4\%)^2 + (1.5\%)^2} = 2.8\%$	$\sqrt{(2.4\%)^2 + (0.4\%)^2} = 2.4\%$
$E = 250 \text{ GeV}$ $\vartheta = 25^\circ$ $Q^2 = 25'700 \text{ GeV}^2$ $x = 0.51$	$\sqrt{(0.76\%)^2 + (0.071\%)^2} = 0.76\%$	$\sqrt{(0.76\%)^2 + (0.020\%)^2} = 0.76\%$
	$\vartheta_{Clu} : \frac{\delta x}{x}$	$\vartheta_Z : \frac{\delta x}{x}$
$E = 25 \text{ GeV}$ $\vartheta = 156^\circ$ $Q^2 = 117 \text{ GeV}^2$ $x = 0.012$	$\sqrt{(21\%)^2 + (1\%)^2} = 21\%$	$\sqrt{(21\%)^2 + (0.3\%)^2} = 21\%$
$E = 250 \text{ GeV}$ $\vartheta = 25^\circ$ $Q^2 = 25'700 \text{ GeV}^2$ $x = 0.51$	$\sqrt{(1.3\%)^2 + (1.0\%)^2} = 1.7\%$	$\sqrt{(1.3\%)^2 + (0.29\%)^2} = 1.4\%$

List of Figures

1.1	Feynman diagrams	7
2.1	Basic diagram for deep inelastic scattering	8
2.2	Lines of constant electron scattering angle	10
2.3	Lines of constant scattered electron energy	11
2.4	Lines of constant current jet angle	12
2.5	Lines of constant current jet energy	13
3.1	The HERA storage ring	15
3.2	The H1 Detector	17
3.3	The central tracking system	19
4.1	From the Geiger Müller counter to the MWPC	20
4.2	Scheme of a drift chamber	21
4.3	The central inner z -chamber CIZ	22
4.4	Isochrones and drift directions in the CIZ	23
4.5	Illustration of the charge division mechanism	24
4.6	Scheme of the Qt -analysis	26
4.7	The different timing methods	27
5.1	CIZ-hits lost by the charge-time analysis	28
5.2	CIZ drift time distribution	29
5.3	Efficiency of CIZ- Qt -old versus CIZ- Qt -corr	32
5.4	Efficiency of CIZ- Qt -corr versus COZ- Qt	33
5.5	Efficiency of CIZ- Qt -corr versus COZ- Qt	33
5.6	φ -resolution of the CIZ- and COZ- Qt	34

5.7	φ -resolution versus integration length	35
5.8	z -resolution of the CIZ- and COZ- Qt	36
6.1	A typical high- Q^2 -event	39
6.2	ϑ -distribution of the simulated event-sample.	40
6.3	Monte-Carlo ϑ -resolutions	44
6.4	Data ϑ -resolutions	45
6.5	ϑ -resolution versus φ	46
6.6	ϑ -resolution versus ϑ	46
6.7	Distributions with respect to a cut ' $\Delta\vartheta < 0.003$ '	48
6.8	Distributions with respect to a cut ' $\Delta\vartheta < 0.003$ '	49
6.9	Energy distribution with respect to a cut ' $\Delta\vartheta < 0.003$ '	50
6.10	ϑ -resolution with respect to a ' $\sigma_{zVert} < 0.33$ '	51

Acknowledgments

I would like to thank the many people I had interesting and fruitful discussion with during the work on this thesis. In particular, I would like to express my gratitude to:

- Ueli Straumann for many discussions on physics and about everything under the sun.
- Katharina Müller and Martin zur Nedden for giving many tips about exploring physics and the famous city of Hamburg.
- Peter Robmann for clarifying many technical details of the CIZ.
- Hanspeter Beck and Stephan Egli for guiding through the labyrinth called H1-software.
- Josef Riedlberger, Monika Wagener, David Müller, Claude Seywert and Roland Bernet for many advice in physics and entertaining hours besides the work.
- Last, but not least, Prof. Dr. P. Truöl, who made this interesting and instructive year in Hamburg possible for me.

This list is far too short to be complete. To the many people from the H1 collaboration, the Physics Institute of the University of Zurich and all the others I have not mentioned here:

Thanks!

Curriculum vitae

Personalien:

Name: Walter
Vorname: Thomas Manuel
Geboren: 23. Februar 1969 in Männedorf
Bürgerort: Winterthur, Zürich, Grüningen

Bildungsgang

1976-1984 Primar- und Sekundarschule in Grüningen
1984-1988 Gymnasium Typus C an der
Kantonsschule Zürcher Oberland, Wetzikon
1989-1995 Studium der Physik an der Universität Zürich
Nebenfächer: Mathematik und Informatik
1994-1995 Diplomarbeit in Experimentalphysik unter der Leitung von
Prof. Dr. P. Truöl und Dr. U. Straumann
Titel: "Optimization of the reconstruction codes for
the central inner z-chamber at the H1 experiment"

Dozentenverzeichnis

C. Amsler	K. Bauknecht	D. Brinkmann
E. Brun	St. Egli	R. Engfer
P. Hess	H. Jarchow	H. Keller
W. Kündig	M. Mali	P. F. Meier
H. H. Müller	R. E. Pixley	H. S. Pruys
G. Rasche	H. Richter	J. Roos
G. Scharf	H. Schauer	B. Schmid
N. Straumann	U. Straumann	P. Stucki
P. Truöl	D. Wyler	

Bibliography

- [1] E. D. Bloom et al., Phys. Rev. Lett. **23**, (1969) 930.
- [2] R. P. Feynman, Phys. Rev. **163**, (1969) 1415.
- [3] H. Fritsch, M. Gell-Mann, H. Leutwyler, Phys. Lett. **47B**, (1973) 1346.
- [4] G. Wolf, Deutsches Elektronen Synchrotron, DESY, Hamburg, 1986, DESY 86-089
- [5] Proc. of the workshop "Physics at Hera", eds. W. Buchmüller and G. Ingelman, Hamburg (1991), vol. 1,2.
- [6] I. Abt et al., H1 Collaboration, "The H1 detector at Hera", DESY 93-103
- [7] K. Müller, "Measurement of the proton structure function F_2 at low Bjorken x at the H1 experiment", Ph. D. thesis, University of Zurich (1994)
- [8] J. Feltesse, "Measurement of inclusive differential cross sections", DPhPE 91-22, CEN-Saclay, France
- [9] P. Robmann, "The central inner z -chamber of the H1 experiment", Ph. D. thesis, University of Zurich (1994)
- [10] V. Blobel et al., "The New Tracker Bank Scheme", H1 Software Note 47, 1994